

Detection of Brain Stimuli Using Ramanujan Periodicity Transforms

Pouria Saidi, Azadeh Vosoughi and George Atia

Department of Electrical and Computer Engineering, University of Central Florida, Orlando, FL, 32816 USA

pouria.saidi@knights.ucf.edu; azadeh@ucf.edu; george.atia@ucf.edu

arXiv:1801.09161v2 [eess.SP] 9 Dec 2018

Abstract—Objective: The ability to efficiently match the frequency of the brain’s response to repetitive visual stimuli in real time is the basis for reliable SSVEP-based Brain-Computer-Interfacing (BCI). **Approach:** The detection of different stimuli is posed as a composite hypothesis test, where SSVEPs are assumed to admit a sparse representation in a Ramanujan Periodicity Transform (RPT) dictionary. For the binary case, we develop and analyze the performance of an RPT detector based on a derived generalized likelihood ratio test. Our approach is extended to multi-hypothesis multi-electrode settings, where we capture the spatial correlation between the electrodes using pre-stimulus data. We also introduce a new metric for evaluating SSVEP detection schemes based on their achievable efficiency and discrimination rate tradeoff for given system resources. **Results:** We obtain exact distributions of the test statistic in terms of confluent hypergeometric functions. Results based on extensive simulations with both synthesized and real data indicate that the RPT detector substantially outperforms spectral-based methods. Its performance also surpasses the state-of-the-art Canonical Correlation Analysis (CCA) methods with respect to accuracy and sample complexity in short data lengths regimes crucial for real-time applications. The proposed approach is asymptotically optimal as it closes the gap to a perfect measurement bound as the data length increases. In contrast to existing supervised methods which are highly data-dependent, the RPT detector only uses pre-stimulus data to estimate the per-subject spatial correlation, thereby dispensing with considerable overhead associated with data collection for a large number of subjects and stimuli. **Significance:** Our work advances the theory and practice of emerging real-time BCI and affords a new framework for comparing SSVEP detection schemes across a wider spectrum of operating regimes.

Index Terms—Ramanujan periodicity transform, Nested periodic matrices, Steady-state visual evoked potentials, Brain computer interface, error exponent-discrimination rate tradeoff.

I. INTRODUCTION

BRAIN computer interfacing (BCI) is used to connect the human nervous system to external devices. Pushing the frontiers of such technology holds promise to assist, and improve the quality of life of, patients with motor disability due to various neurological disorders through the use of intention-controlled prosthetics. Non-invasive BCIs exploit features from Electroencephalogram (EEG) signals distinctive of different tasks. For example, motor imagery BCI refers to a class of BCI in which features and patterns are extracted from EEG sensorimotor rhythms triggered by action imagination (e.g., imagined movement of the limbs). Despite noteworthy efforts to devise a host of techniques to classify EEG trials

associated with movement imagination [1], [2], motor imagery BCI remains at its infancy to date.

Evoked-potential-based BCI is another non-invasive technology that records EEG signals from electrical activity induced on the cortex in response to some repetitive visual stimulus using electrodes attached to the scalp. The brain’s responses to such external stimuli, known as Steady State Visual Evoked Potential (SSVEPs), are known to exhibit periodicity matching that of the stimuli [3]. The (quasi) periodic patterns of SSVEPs have been the basis for much progress in the theory and practice of SSVEP-BCI. For example, spectral-based methods capturing the energy distribution across the frequency spectrum such as Power Spectral Density Analysis (PSDA) are popular choices for classifying SSVEPs [3], [4]. However, the presence of high levels of background noise due to brain chatter – inevitably superimposed on the recorded brain’s response – continues to be a major challenge in face of the development of reliable SSVEP detectors. Its degrading effect on performance is further compounded by the stringent and indispensable latency requirements of real-time BCI, in which high levels of accuracy are mandated with short delay. For instance, the frequency resolution of spectral-based methods is severely diminished with the use of shorter data lengths.

An alternative and state-of-the-art approach to SSVEP detection relies on Canonical Correlation Analysis (CCA) – initially proposed in [5] to find relations between sets of variates. In particular, the authors in [6] leveraged CCA in developing a method for SSVEP classification, which we refer to in this work as standard CCA. The key idea underlying standard CCA is obtaining the maximum correlation of the data with a reference matrix defined for each class consisting of periodic signals with the frequency of the stimulus and its harmonics to decide on a class label. Some of the state-of-the-art supervised algorithms originated from standard CCA such as in [7]–[10] to further boost the performance of SSVEP classification, albeit at the expense of heavy reliance on post-stimulus training trials [11]. One drawback of excessive reliance on such data in the training phase of supervised methods, such as Individual Template CCA (IT CCA), lies in the overhead and cost associated with data collection. For example, the low-frequency flashing lights in SSVEP-based BCIs used to obtain large amplitude responses on the brain cortex [12] could become tiring and burdensome for some subjects, may cause eye fatigue, and may even trigger seizures in some patients [13], [14].

Other than the use of Fourier transform and periodograms to identify periodic signals intrinsic to time series-data (as in PSDA), there exist periodicity estimation methods that search for periodicities and regularities in data directly in the time domain [15], [16]. For example, the authors in [17] studied periodicity estimation using representations of discrete periodic sequences in Nested Periodic Matrices (NPMs). They also introduced the so-called Ramanujan Periodicity Transforms (RPT) as an instance of NPMs. The use of RPT was shown to exhibit robustness to noise and phase shifts. Ramanujan sums defining the bases for RPT were shown useful in representing periodic sequences in various applications [18]. However, only few works have investigated their application with biomedical signals, such as in the analysis of T-wave alternans [19] and the detection of tandem repeats in DNA [20]. We leveraged an RPT-based model to detect SSVEPs for the first time in [21], [22] providing preliminary results for the current work, and demonstrated its ability to capture the underlying periodicity in SSVEPs and its robustness to latencies naturally present in the brain's response to external stimuli.

Contributions: In this paper, we build on our preliminary prior work on the RPT model and extensively analyze SSVEP detection in a composite hypothesis testing framework. The following summarizes the main contributions of this paper.

- We develop an RPT detector of the brain's response associated with various stimuli based on a generalized likelihood ratio test (GLRT) under the proposed RPT model.
- We provide an exact analysis of the performance of the RPT detector by deriving the distributions of the test statistic characterized in terms of confluent hypergeometric functions for the binary case.
- We devise flexible Gaussian approximations of the derived distributions that avail an efficient framework for the design of stimulus waveforms for high-accuracy BCIs.
- We establish asymptotic optimality of the proposed approach by analyzing the performance gap with respect to a derived perfect measurement bound for the composite test. The gap is shown to vanish exponentially fast in the EEG system resources (data length L and signal to noise ratio (SNR)).
- We introduce and investigate the tradeoff between the error exponent, $-\log P_e / (L \cdot \text{SNR})$, capturing the rate at which the classification error decays with L and SNR and the discrimination rate $\log_2 M$ (the logarithm of the number of classes being discriminated) for various detection methods including the RPT detector for a given number of electrodes. Inspired by the concept of diversity and multiplexing from communication theory [23], this tradeoff is introduced here for the first time in the context of SSVEP detection and is shown to be particularly useful for comparing various detection methodologies across an entire spectrum of operation regimes.
- We extend our approach and derive the corresponding test for multi-hypothesis and multi-channel settings, where we capture the spatial correlation between the recording electrodes.

The paper is organized as follows. In section II, we provide a brief background about Ramanujan sums and RPT matrices and their properties. Then, we present the composite hypothesis testing model, and provide an analysis of the RPT detector and the associated sufficient statistic for the binary case. The analysis is extended to multi-class and multi-electrode settings. We present our results on synthesized and real data in Section III. Section IV is devoted to a discussion and our concluding remarks are in Section V.

II. METHODS

Notation: We use lowercase letters for scalars, bold lowercase letters for vectors and bold uppercase letters for matrices. We use $d|T$ to indicate that d is a divisor of T . The Euler totient function of p , that is the number of positive integers smaller than p that are co-prime to p , is denoted by $\phi(p)$. Given a set S , the set S^c denotes its complement. The operator $\text{tr}(\cdot)$ denotes the trace of its matrix argument, and \log denotes the natural logarithm to the base e , unless the base is made explicit. We use the notation $\mathbf{x} \sim \mathcal{N}(\mu, \Sigma)$ to indicate that a random vector \mathbf{x} has a multivariate normal (Gaussian) distribution with mean vector μ and covariance matrix Σ .

A. Ramanujan Sums and RPT Dictionary

In [17], the authors introduced NPMs that can capture periodicity in sequences. They extended the notion of these matrices to periodicity dictionaries. In [24], periodicity dictionaries of order P_{\max} are defined as the set of signals \mathcal{B} that can represent all periodic sequences with period $1 \leq p \leq P_{\max}$ through linear combinations of signals in the set \mathcal{B} . It was shown that a dictionary that spans all subspaces of periodic signals of periods 1 to P_{\max} must contain at least $\phi(p)$ linearly independent signals with period p for each p . Consequently, a periodic dictionary of order P_{\max} must have at least $\sum_{p=1}^{P_{\max}} \phi(p)$ linearly independent signals.

RPT matrices are instances of the NPMs built from Ramanujan sums [25]. A Ramanujan sum is defined as

$$c_q(n) = \sum_{\substack{k=1 \\ (k,q)=1}}^q e^{j2\pi kn/q}, \quad (1)$$

where (k, q) is the greatest common divisor (gcd) of k and q . The sequence $c_q(n)$ is an all integer, symmetric and periodic sequence with period q . For instance, $c_1(n) = \{1\}$, $c_2(n) = \{1, -1\}$, $c_3(n) = \{2, -1, -1\}$, $c_4(n) = \{2, 0, -2, 0\}$ and $c_5(n) = \{4, -1, -1, -1, -1\}$. These examples show only one period of the sequences. Properties of Ramanujan sums are investigated in [26] and [27]. One important feature of $c_q(n)$ highly relevant to our work is the orthogonality property. Specifically, the sequences $c_{q_1}(n)$ and $c_{q_2}(n)$ are orthogonal over the sequence length $L = \text{lcm}(q_1, q_2)$ for $q_1 \neq q_2$, where lcm is the least common multiplier of q_1 and q_2 , i.e.,

$$\sum_{n=0}^{L-1} c_{q_1}(n)c_{q_2}(n-k) = 0, \quad q_1 \neq q_2 \quad (2)$$

for any integer $0 \leq k \leq L-1$.

We define the sequence \mathbf{c}_q

$$\mathbf{c}_q = [c_q(0) \quad c_q(1) \quad \dots \quad c_q(q-1)]^T.$$

For each $1 \leq q \leq P_{\max}$, a submatrix \mathbf{C}_q is constructed from columns that are circularly downshifted versions of \mathbf{c}_q , i.e.,

$$\mathbf{C}_q = \begin{bmatrix} \mathbf{c}_q & \mathbf{c}_q^{(1)} & \dots & \mathbf{c}_q^{(\phi(q)-1)} \end{bmatrix}, \quad (3)$$

where $\mathbf{c}_q^{(1)}$ is the circularly downshifted version of \mathbf{c}_q , i.e.,

$$\mathbf{c}_q^{(1)} = [c_q(q-1) \quad c_q(0) \quad c_q(1) \quad \dots \quad c_q(q-2)]^T. \quad (4)$$

The versions $\mathbf{c}_q^{(i)}$ are similarly defined with higher order downshifts. For instance, \mathbf{C}_4 and \mathbf{C}_5 are

$$\mathbf{C}_4 = \begin{bmatrix} 2 & 0 \\ 0 & 2 \\ -2 & 0 \\ 0 & -2 \end{bmatrix}_{4 \times \phi(4)} \quad \mathbf{C}_5 = \begin{bmatrix} 4 & -1 & -1 & -1 \\ -1 & 4 & -1 & -1 \\ -1 & -1 & 4 & -1 \\ -1 & -1 & -1 & 4 \\ -1 & -1 & -1 & -1 \end{bmatrix}_{5 \times \phi(5)} \quad (5)$$

We extend the matrices \mathbf{C}_q periodically to length L yielding submatrices \mathbf{R}_q . We can readily define the RPT dictionary matrix \mathbf{K} [24] constructed by concatenating all submatrices $\mathbf{R}_q, q = 1, \dots, P_{\max}$, where P_{\max} is the largest possible value that q assumes. Thus,

$$\mathbf{K} = [\mathbf{R}_1 \quad \mathbf{R}_2 \quad \mathbf{R}_3 \quad \dots \quad \mathbf{R}_{P_{\max}}]. \quad (6)$$

Such dictionaries are called Nested Periodic Dictionaries (NPD). We note that NPDs have exactly $\phi(p)$ signals with period p for each p . In the next two sections, we develop the SSVEP detection problem in a composite hypothesis testing framework using the signal representations in an RPT dictionary and analyze the performance of the developed detector.

B. Binary SSVEP Detection

1) *Composite binary hypothesis testing model:* In this section, we assume that the SSVEP is associated with one of two stimuli with frequencies f_0 and f_1 , which represent two possible hypotheses H_0 and H_1 , respectively. Equivalently, the recorded sequence is of period T_0 or T_1 . We consider an observation model in which we express the measurements under each of the hypotheses using the model,

$$\begin{aligned} H_0 : \mathbf{y} &= \mathbf{K}\mathbf{x}_0 + \mathbf{w} \\ H_1 : \mathbf{y} &= \mathbf{K}\mathbf{x}_1 + \mathbf{w} \end{aligned} \quad (7)$$

where \mathbf{y} is an $L \times 1$ observation (measurement) vector, \mathbf{K} is the $L \times \sum_{p=1}^{P_{\max}} \phi(p)$ RPT dictionary matrix (L is the length of the sequences), \mathbf{x}_0 and \mathbf{x}_1 are the $\sum_{p=1}^{P_{\max}} \phi(p) \times 1$ representations of the observations in the RPT subspace, modeled as two deterministic but unknown vectors. The $L \times 1$ vector \mathbf{w} is an additive white Gaussian noise (AWGN) vector with covariance matrix $\sigma^2 \mathbf{I}$ modeling the background EEG noise, that is, $\mathbf{w} \sim \mathcal{N}(0, \sigma^2 \mathbf{I})$. Given \mathbf{x}_m we can write the distribution of \mathbf{y} as $\mathbf{y} \sim \mathcal{N}(\mathbf{K}\mathbf{x}_m, \sigma^2 \mathbf{I})$, where $m \in \{0, 1\}$. Reference [17] considers a period *estimation* problem where the support set (locations of the nonzero entries) of the signal representation is unknown. By contrast, here we incorporate prior information

about the support of \mathbf{x}_0 and \mathbf{x}_1 under both hypotheses since the period of the SSVEP should match that of the stimulus. We denote the known support sets $\text{supp}(\mathbf{x}_m)$ for \mathbf{x}_m by $S_m := \{j : x_{m,j} \neq 0\}$, where $x_{m,j}$ is the j -th element of \mathbf{x}_m , $m = 0, 1$. The non-zero elements correspond to the columns of the submatrices of \mathbf{K} associated with period T_m and its divisors. We define \mathbf{K}_{S_m} whose columns are the columns of \mathbf{K} indexed by the support set S_m , and column vector \mathbf{x}_{S_m} whose entries are equal to the non-zero entries of \mathbf{x}_m indexed by S_m . We define the SNR corresponding to hypothesis H_m as

$$\text{SNR}_m = \frac{\mathbf{x}_{S_m}^T \mathbf{K}_{S_m}^T \mathbf{K}_{S_m} \mathbf{x}_{S_m}}{\sigma^2 L}. \quad (8)$$

Without loss of generality, we set $\sigma^2 = 1$ so that different SNRs can be accounted for by varying the magnitude of the signal part on the support.

2) *Binary RPT detector:* Let $f(\mathbf{y}|H_m)$ denote the conditional probability density function (pdf) of the measurement vector \mathbf{y} given hypothesis H_m . For the model in (7) we can write:

$$f(\mathbf{y}|H_m) = \frac{1}{(2\pi\sigma^2)^{\frac{L}{2}}} \exp\left(-\frac{\|\mathbf{y} - \mathbf{K}\mathbf{x}_m\|_2^2}{2\sigma^2}\right). \quad (9)$$

The binary RPT detector is obtained from the GLRT defined as [28]

$$\mathcal{L}(\mathbf{y}) = \frac{\max_{\mathbf{x}_1: \text{supp}(\mathbf{x}_1)=S_1} f(\mathbf{y}|H_1)}{\max_{\mathbf{x}_0: \text{supp}(\mathbf{x}_0)=S_0} f(\mathbf{y}|H_0)} \underset{H_0}{\overset{H_1}{\geq}} \eta, \quad (10)$$

which requires computing the restricted Maximum Likelihood (ML) estimate of \mathbf{x}_m when the support set is restricted to S_m . From (9), the restricted ML estimate under $H_m, m = 0, 1$, is obtained as the solution to

$$\min_{\mathbf{x}_m: \text{supp}(\mathbf{x}_m)=S_m} \|\mathbf{y} - \mathbf{K}\mathbf{x}_m\|_2^2. \quad (11)$$

Accordingly, we can rewrite (11) as

$$\min \|\mathbf{y} - \mathbf{K}_{S_m} \mathbf{x}_{S_m}\|_2^2. \quad (12)$$

The solution to (12) can be expressed as

$$\hat{\mathbf{x}}_{S_m} = (\mathbf{K}_{S_m}^T \mathbf{K}_{S_m})^{-1} \mathbf{K}_{S_m}^T \mathbf{y}. \quad (13)$$

Replacing in (10), the decision rule reduces to

$$\ell(\mathbf{y}) = \mathbf{y}^T \mathbf{B} \mathbf{y} - \mathbf{y}^T \mathbf{A} \mathbf{y} \underset{H_0}{\overset{H_1}{\geq}} 2\sigma^2 \log \eta = \gamma, \quad (14)$$

where $\mathbf{B} = \mathbf{K}_{S_1} (\mathbf{K}_{S_1}^T \mathbf{K}_{S_1})^{-1} \mathbf{K}_{S_1}^T$, $\mathbf{A} = \mathbf{K}_{S_0} (\mathbf{K}_{S_0}^T \mathbf{K}_{S_0})^{-1} \mathbf{K}_{S_0}^T$ and $\ell(\mathbf{y})$ is the sufficient statistic. The two matrices \mathbf{A} and \mathbf{B} in (14) are idempotent, i.e., $\mathbf{A}^2 = \mathbf{A}, \mathbf{B}^2 = \mathbf{B}$ and their eigenvalues are either 0 or 1.

3) *Performance analysis of the binary RPT detector:* In this section, we analyze the performance of the detector in (14). We start off with the special case where the length of \mathbf{y} (measured in number of sample) is $L = \text{lcm}(T_0, T_1)$. In this case, the orthogonality of the RPT sub-matrices is preserved. Under this assumption, we are able to obtain the exact distributions of the test statistic $\ell(\mathbf{y})$, and in turn provide an exact performance analysis. Then, we consider the general case in which \mathbf{y} is

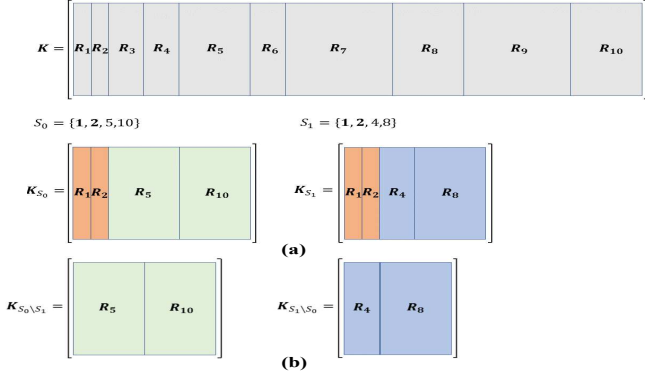


Fig. 1. (a) Schematic for an example of the RPT dictionary matrix \mathbf{K} and its submatrices, where $T_0 = 10$ and $T_1 = 8$. (b) RPT matrices are restricted to support sets S_0 and S_1 . In this example, \mathbf{R}_1 and \mathbf{R}_2 exist in both \mathbf{K}_{S_0} and \mathbf{K}_{S_1} matrices.

of arbitrary length L . In this case, the orthogonality of the RPT submatrices is not necessarily preserved. For the general case, we provide an approximate analysis based on Gaussian approximations of the distributions of $\ell(\mathbf{y})$.

• *Orthogonal case when $L = \text{lcm}(T_0, T_1)$* : If the periods T_0 and T_1 share any divisors, the support sets S_0 and S_1 are non-disjoint, i.e., $S_0 \cap S_1 \neq \emptyset$. Therefore, the decision rule in (14) reduces to

$$\ell(\mathbf{y}) = \mathbf{y}^T \mathbf{B}^\perp \mathbf{y} - \mathbf{y}^T \mathbf{A}^\perp \mathbf{y} \underset{H_0}{\underset{H_1}{\geq}} 2\sigma^2 \log \eta = \gamma, \quad (15)$$

where the matrices \mathbf{A}^\perp and \mathbf{B}^\perp are given by

$$\begin{aligned} \mathbf{A}^\perp &= \mathbf{K}_{S_0 \setminus S_1} (\mathbf{K}_{S_0 \setminus S_1}^T \mathbf{K}_{S_0 \setminus S_1})^{-1} \mathbf{K}_{S_0 \setminus S_1}^T \\ \mathbf{B}^\perp &= \mathbf{K}_{S_1 \setminus S_0} (\mathbf{K}_{S_1 \setminus S_0}^T \mathbf{K}_{S_1 \setminus S_0})^{-1} \mathbf{K}_{S_1 \setminus S_0}^T, \end{aligned} \quad (16)$$

and $S_i \setminus S_j$ denotes the difference set of S_i and S_j . The superscript \perp is reserved for this orthogonal case throughout this subsection. Fig. 1(a) shows a schematic of the dictionary matrix \mathbf{K} and its submatrices in which $T_0 = 10$ and $T_1 = 8$. Fig. 1(b) illustrates the RPT matrices that are restricted to support sets S_0 and S_1 and also submatrices $\mathbf{K}_{S_0 \setminus S_1}$ and $\mathbf{K}_{S_1 \setminus S_0}$ corresponding to two difference sets $S_0 \setminus S_1$ and $S_1 \setminus S_0$, respectively. As shown, the submatrices \mathbf{R}_1 and \mathbf{R}_2 corresponding to the divisors 1 and 2, respectively, exist in both \mathbf{K}_{S_0} and \mathbf{K}_{S_1} , thus do not play a role in the sufficient statistic. Per the definitions of \mathbf{A}^\perp and \mathbf{B}^\perp in (16), the measurement vector \mathbf{y} is projected onto the column space of $\mathbf{K}_{S_0 \setminus S_1}$ and $\mathbf{K}_{S_1 \setminus S_0}$, and the decision rule in (15) chooses the index of the subspace that yields the larger projection. This insight is demonstrated in Fig. 2. In Fig. 2(a), we have $L = \text{lcm}(T_0, T_1)$ and thus the orthogonality of the RPT subspaces is preserved, and in Fig. 2(b) L is arbitrary and therefore the subspaces are not orthogonal. We have the following lemma.

Lemma 1. For $L = \text{lcm}(T_0, T_1)$, we have $\mathbf{A}^\perp \mathbf{B}^\perp = \mathbf{0}$.

Proof. Lemma 1 follows from the orthogonality property in (2), which for the choice of $L = \text{lcm}(T_0, T_1)$ ensures that the columns of submatrices \mathbf{K}_{S_0} and \mathbf{K}_{S_1} corresponding to distinct divisors are orthogonal. Since the submatrices $\mathbf{K}_{S_0 \setminus S_1}$ and $\mathbf{K}_{S_1 \setminus S_0}$ of the RPT dictionary \mathbf{K} indexed by the difference

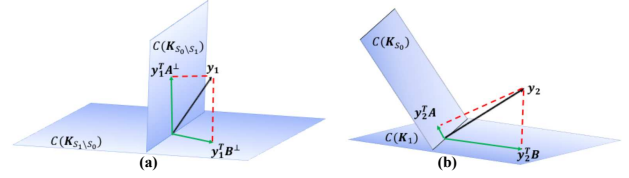


Fig. 2. (a) For $L = \text{lcm}(T_0, T_1)$, the column spaces $\mathcal{C}(\mathbf{K}_{S_0 \setminus S_1})$ and $\mathcal{C}(\mathbf{K}_{S_1 \setminus S_0})$ of the orthogonal submatrices effective in the decision rule are orthogonal. The GLRT chooses the index corresponding to the subspace that yields the larger projection. Here, $\mathbf{y}_1^T \mathbf{A}^\perp \mathbf{y}_1 > \mathbf{y}_1^T \mathbf{B}^\perp \mathbf{y}_1$, hence the RPT detector maps \mathbf{y}_1 to H_0 . (b) For arbitrary L , the submatrices are not orthogonal. Since, $\mathbf{y}_2^T \mathbf{A}^\perp \mathbf{y}_2 < \mathbf{y}_2^T \mathbf{B}^\perp \mathbf{y}_2$, the RPT detector maps \mathbf{y}_2 to H_1 .

sets do not share any columns, we have $\mathbf{K}_{S_0 \setminus S_1}^T \mathbf{K}_{S_1 \setminus S_0} = \mathbf{0}$, hence, $\mathbf{A}^\perp \mathbf{B}^\perp = \mathbf{0}$. \square

To analyze the performance of the RPT detector, we need $f(\ell(\mathbf{y})|H_0)$ and $f(\ell(\mathbf{y})|H_1)$, the pdfs of the test statistic $\ell(\mathbf{y})$ under each hypothesis. From [29, Lemma 1.1] it follows that the two quadratic terms $\mathbf{y}^T \mathbf{A}^\perp \mathbf{y}$ and $\mathbf{y}^T \mathbf{B}^\perp \mathbf{y}$ in (15) have Chi-squared distributions $\chi^2(r_A^\perp, \lambda_{m,A}^{2,\perp})$ and $\chi^2(r_B^\perp, \lambda_{m,B}^{2,\perp})$ under hypothesis H_m , where r_A^\perp and r_B^\perp are the degrees of freedom, and $\lambda_{m,A}^{2,\perp}$ and $\lambda_{m,B}^{2,\perp}$ are the non-centrality parameters. From [30], we can readily state the following theorem proved in Appendix A, which provides exact expressions for the distributions of the sufficient statistic $\ell(\mathbf{y})$ for the orthogonal case when $L = \text{lcm}(T_0, T_1)$.

Theorem 2. (Distribution of test statistic for orthogonal case) The distributions $f(\ell(\mathbf{y})|H_m)$, $m = 0, 1$, of the sufficient statistic $\ell(\mathbf{y}) = \mathbf{y}^T \mathbf{B}^\perp \mathbf{y} - \mathbf{y}^T \mathbf{A}^\perp \mathbf{y}$ in (15) are given by

$$\begin{aligned} f(\ell(\mathbf{y})|H_1) &= \sum_{i=0}^{\infty} \frac{\exp(-\frac{1}{2}\lambda_{1,B}^{2,\perp})(\lambda_{1,B}^{2,\perp}/2)^i}{i!} p_{r_B^\perp+2i, r_A^\perp}(t) \\ f(\ell(\mathbf{y})|H_0) &= \sum_{j=0}^{\infty} \frac{\exp(-\frac{1}{2}\lambda_{0,A}^{2,\perp})(\lambda_{0,A}^{2,\perp}/2)^j}{j!} p_{r_B^\perp, r_A^\perp+2j}(t) \end{aligned} \quad (17)$$

where

$$p_{a,b}(t) = \begin{cases} \frac{2^{-\frac{(a+b)}{2}}}{\Gamma(a/2)} t^{\frac{a+b-2}{2}} e^{-\frac{t}{2}} \psi\left(\frac{b}{2}, \frac{a+b}{2}; t\right) & \text{if } t \geq 0 \\ \frac{2^{-\frac{(a+b)}{2}}}{\Gamma(b/2)} (-t)^{\frac{a+b-2}{2}} e^{\frac{t}{2}} \psi\left(\frac{a}{2}, \frac{a+b}{2}; -t\right) & \text{if } t \leq 0 \end{cases} \quad (18)$$

and $\psi(a, b; x)$ is defined as

$$\psi(a, b; x) = (\Gamma(a))^{-1} \int_0^\infty e^{-xt} t^{a-1} (1+t)^{b-a-1} dt, \quad (19)$$

and the parameters of the non-central Chi-squared distributions are

$$\begin{aligned} \lambda_{0,A}^{2,\perp} &= \sum_{\substack{i=1 \\ d_i \notin T_1}}^v \mathbf{x}_{S_0,i}^T \mathbf{K}_{S_0,i}^T \mathbf{K}_{S_0,i} \mathbf{x}_{S_0,i}, & \lambda_{1,A}^{2,\perp} &= 0 \\ \lambda_{1,B}^{2,\perp} &= \sum_{\substack{j=1 \\ d_j \notin T_0}}^u \mathbf{x}_{S_1,j}^T \mathbf{K}_{S_1,j}^T \mathbf{K}_{S_1,j} \mathbf{x}_{S_1,j}, & \lambda_{0,B}^{2,\perp} &= 0 \\ r_A^\perp &= \sum_{\substack{i=1 \\ d_i \notin T_1}}^v \phi(d_i|T_0) & r_B^\perp &= \sum_{\substack{j=1 \\ d_j \notin T_0}}^u \phi(d_j|T_1) \end{aligned} \quad (20)$$

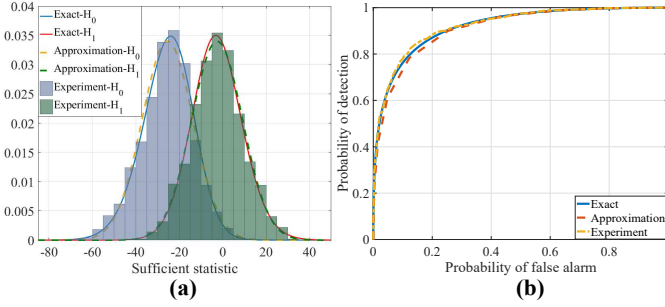


Fig. 3. (a) The exact and Gaussian approximated distributions of $\ell(\mathbf{y})$ derived in (17) and (21) are in agreement and match the histogram of $\ell(\mathbf{y})$ obtained from numerical experiments. (b) The ROC curve obtained from numerical integration of the exact pdfs is close to the ones obtained from the Gaussian approximated pdfs and from the numerical experiment.

where \mathcal{T}_0 and \mathcal{T}_1 are the sets of divisors of T_0 and T_1 of cardinalities v and u , respectively, $\mathbf{K}_{S_{0,i}}$, $i = 1, \dots, v$, and $\mathbf{K}_{S_{1,j}}$, $j = 1, \dots, u$, are the corresponding submatrices, and $\mathbf{x}_{S_{m,i}}$ and $\mathbf{x}_{S_{m,j}}$ are rows of \mathbf{x}_{S_m} restricted to the index set of the i -th and j -th divisors of T_0 and T_1 .

Proof. Per Lemma 1 and Theorem 2, the sufficient statistic $\ell(\mathbf{y})$ in (15) is the difference of two independent non-central Chi-squared random variables (RVs). Accordingly, the proof of Theorem 2 follows from Theorems 2.1B, 3.1, 3.2, 3.3 in [30] which characterize the distribution of linear combinations of independent non-central Chi-squared RVs in terms of confluent hypergeometric functions. Further details are provided in Appendix A. \square

In designing BCIs, it is desirable to select waveforms that yield well-separable hypotheses with respect to the employed signals representation. Due to the complexity of the exact pdf expressions of the sufficient statistic $\ell(\mathbf{y})$ in (17), we approximate these pdfs with Gaussian distributions by fitting the first and second order statistics. These Gaussian approximations lead to a flexible waveform design. Recalling that a non-central Chi-squared distribution with r degrees of freedom and non-centrality parameter λ^2 has a mean $r + \lambda^2$ and variance $2(r + 2\lambda^2)$, the approximate Gaussian pdfs under H_0 and H_1 are

$$\begin{aligned} H_0 : \ell(\mathbf{y}) &\sim \mathcal{N}\left(r_B^\perp - r_A^\perp - \lambda_{0,A}^{2,\perp}, 2(r_B^\perp + r_A^\perp) + 4\lambda_{0,A}^{2,\perp}\right) \\ H_1 : \ell(\mathbf{y}) &\sim \mathcal{N}\left(r_B^\perp - r_A^\perp + \lambda_{1,B}^{2,\perp}, 2(r_B^\perp + r_A^\perp) + 4\lambda_{1,B}^{2,\perp}\right) \end{aligned} \quad (21)$$

To validate these theoretical results, we consider (7) and assume that the periods corresponding to the two stimuli are $T_0 = 32$, $T_1 = 18$ under hypotheses H_0 and H_1 , respectively. We fix SNR = -14 dB and generate 2000 observation vectors \mathbf{y} under each hypothesis. Fig. 3(a) shows that the exact pdfs of $\ell(\mathbf{y})$ under H_0 and H_1 derived in (17) agree with the approximated Gaussian pdfs in (21) and histograms of the sufficient statistic $\ell(\mathbf{y})$ obtained from numerical experiments. Based on these Gaussian approximations, we can obtain the probability of detection $P_D := \mathbb{P}_1(\ell(\mathbf{y}) > \gamma)$ and the probability of false alarm $P_F := \mathbb{P}_0(\ell(\mathbf{y}) > \gamma)$, where \mathbb{P}_m

denotes the probability measure under the m -th hypothesis

$$\begin{aligned} P_D &= Q\left(\frac{\gamma - r_B^\perp + r_A^\perp - \lambda_{1,B}^{2,\perp}}{\sqrt{(2(r_B^\perp + r_A^\perp) + 4\lambda_{1,B}^{2,\perp})}}\right) \\ P_F &= Q\left(\frac{\gamma - r_B^\perp + r_A^\perp + \lambda_{0,A}^{2,\perp}}{\sqrt{(2(r_B^\perp + r_A^\perp) + 4\lambda_{0,A}^{2,\perp})}}\right) \end{aligned} \quad (22)$$

where $Q(\cdot)$ denotes the Q-function, which is the tail of the standard Normal distribution. Fig. 3(b) illustrates the ROC curves, where P_D and P_F corresponding to the exact pdfs are obtained using numerical integration of the exact pdfs in (17), and P_D and P_F corresponding to the approximate Gaussian pdfs in (21) are found using (22). Clearly, the ROC curves are in close agreement.

•*General case when L is arbitrary:* In this section, we treat the general case with arbitrary L that does not necessarily lead to orthogonality. The two quadratic terms $\mathbf{y}^T \mathbf{A} \mathbf{y}$ and $\mathbf{y}^T \mathbf{B} \mathbf{y}$ have χ^2 distributions $\chi^2(r_A, \lambda_{m,A}^2)$ and $\chi^2(r_B, \lambda_{m,B}^2)$ under hypotheses H_m , $m = 0, 1$. The parameters of these distributions can be written as

$$\begin{aligned} \lambda_{0,A}^2 &= \mathbf{x}_{S_0}^T \mathbf{K}_{S_0}^T \mathbf{A} \mathbf{K}_{S_0} \mathbf{x}_{S_0} = \mathbf{x}_{S_0}^T \mathbf{K}_{S_0}^T \mathbf{K}_{S_0} \mathbf{x}_{S_0} \\ \lambda_{0,B}^2 &= \mathbf{x}_{S_0}^T \mathbf{K}_{S_0}^T \mathbf{B} \mathbf{K}_{S_0} \mathbf{x}_{S_0} \\ \lambda_{1,A}^2 &= \mathbf{x}_{S_1}^T \mathbf{K}_{S_1}^T \mathbf{A} \mathbf{K}_{S_1} \mathbf{x}_{S_1} \\ \lambda_{1,B}^2 &= \mathbf{x}_{S_1}^T \mathbf{K}_{S_1}^T \mathbf{B} \mathbf{K}_{S_1} \mathbf{x}_{S_1} = \mathbf{x}_{S_1}^T \mathbf{K}_{S_1}^T \mathbf{K}_{S_1} \mathbf{x}_{S_1} \\ r_A &= \sum_{i=1}^v \phi(d_i | T_0) = T_0 \quad r_B = \sum_{j=1}^u \phi(d_j | T_1) = T_1 \end{aligned} \quad (23)$$

Since L is arbitrary, the two random variables $\mathbf{y}^T \mathbf{A} \mathbf{y}$ and $\mathbf{y}^T \mathbf{B} \mathbf{y}$ are not necessarily orthogonal, wherefore they are not independent and finding the exact pdf of $\ell(\mathbf{y})$ requires obtaining the joint pdf of these two dependent/correlated RVs. Akin to the orthogonal case, we approximate the pdf of $\ell(\mathbf{y})$ with a Gaussian distribution by fitting the first and second order statistics and considering the covariance between the two RVs $\mathbf{y}^T \mathbf{A} \mathbf{y}$ and $\mathbf{y}^T \mathbf{B} \mathbf{y}$ for the test statistic under each hypothesis. Therefore, we consider the approximate model

$$\begin{aligned} H_0 : \ell(\mathbf{y}) &\sim \mathcal{N}(r_B - r_A + \lambda_{0,B}^2 - \lambda_{0,A}^2, \sigma_0^2) \\ H_1 : \ell(\mathbf{y}) &\sim \mathcal{N}(r_B - r_A + \lambda_{1,B}^2 - \lambda_{1,A}^2, \sigma_1^2) \end{aligned} \quad (24)$$

where

$$\begin{aligned} \sigma_0^2 &= 2(r_B + 2\lambda_{0,B}^2) + 2(r_A + 2\lambda_{0,A}^2) \\ &\quad - 2 \text{Cov}(\mathbf{y}^T \mathbf{B} \mathbf{y}, \mathbf{y}^T \mathbf{A} \mathbf{y} | H_0) \\ \sigma_1^2 &= 2(r_B + 2\lambda_{1,B}^2) + 2(r_A + 2\lambda_{1,A}^2) \\ &\quad - 2 \text{Cov}(\mathbf{y}^T \mathbf{B} \mathbf{y}, \mathbf{y}^T \mathbf{A} \mathbf{y} | H_1) \end{aligned} \quad (25)$$

and $\text{Cov}(\mathbf{y}^T \mathbf{B} \mathbf{y}, \mathbf{y}^T \mathbf{A} \mathbf{y} | H_m)$ denotes the covariance between $\mathbf{y}^T \mathbf{A} \mathbf{y}$ and $\mathbf{y}^T \mathbf{B} \mathbf{y}$ under H_m . In Appendix B, we show that

$$\begin{aligned} \text{Cov}(\mathbf{y}^T \mathbf{B} \mathbf{y}, \mathbf{y}^T \mathbf{A} \mathbf{y} | H_0) &= 4\lambda_{0,B}^2 + 2 \sum_{i=1}^L \sum_{j=1}^L c_{ij} \\ \text{Cov}(\mathbf{y}^T \mathbf{B} \mathbf{y}, \mathbf{y}^T \mathbf{A} \mathbf{y} | H_1) &= 4\lambda_{1,A}^2 + 2 \sum_{i=1}^L \sum_{j=1}^L c_{ij} \end{aligned} \quad (26)$$

where c_{ij} is the (i, j) -th entry of matrix $\mathbf{C} = \mathbf{A} \odot \mathbf{B}$, and \odot is an element-wise product. We can readily obtain general expressions for P_D and P_F ,

$$P_D = Q \left(\frac{\gamma - r_B - \lambda_{1,B}^2 + r_A + \lambda_{1,A}^2}{\sqrt{(2(r_B + r_A) + 4(\lambda_{1,B}^2 - \lambda_{1,A}^2) - 4 \sum_{i=1}^L \sum_{j=1}^L c_{ij})}} \right)$$

$$P_F = Q \left(\frac{\gamma - r_B - \lambda_{0,B}^2 + r_A + \lambda_{0,A}^2}{\sqrt{(2(r_B + r_A) + 4(\lambda_{0,A}^2 - \lambda_{0,B}^2) - 4 \sum_{i=1}^L \sum_{j=1}^L c_{ij})}} \right). \quad (27)$$

Under the Neyman-Pearson criteria [28], the maximum value for P_D for false alarm level α , i.e., $P_F \leq \alpha$, is given in (28).

4) *Perfect measurement bound for the binary RPT detector:* In this section, we derive an upper bound on the performance of the proposed binary RPT detector. We use a standard approach from detection theory in which an upper bound on the performance of all composite tests is obtained by assuming that the signals \mathbf{x}_0 and \mathbf{x}_1 are known, hence the appellation ‘perfect measurement bound’ (PMB) [28]. Under this hypothetical assumption, the problem reduces to one of a simple binary hypothesis testing problem. For our problem, under this assumption the optimal test becomes

$$\ell(\mathbf{y}) = \mathbf{y}^T (\mathbf{K}_{S_1} \mathbf{x}_{S_1} - \mathbf{K}_{S_0} \mathbf{x}_{S_0})$$

$$\underset{H_0}{\geq} \ln(\eta) + \frac{1}{2} (\mathbf{x}_{S_1}^T \mathbf{K}_{S_1}^T \mathbf{K}_{S_1} \mathbf{x}_{S_1} - \mathbf{x}_{S_0}^T \mathbf{K}_{S_0}^T \mathbf{K}_{S_0} \mathbf{x}_{S_0}). \quad (30)$$

Given the model in (7), under the Neyman-Pearson criteria, P_D for false alarm level α is expressed in (29). We note that, (29) provides an upper bound on the performance of all composite tests corresponding to the model in (7), including the proposed RPT detector in (14).

To compare the performance of the proposed RPT detector to the PMB, we let $\text{gap}(L, \text{SNR})$ denote the difference between P_D of the RPT detector and the PMB. Lemma 3 provides an approximate characterization of the gap in the asymptotic regime of large L . There are two main sources of approximation, namely using the Gaussian approximate distribution and using an approximation for the Q-function.

Lemma 3. *Suppose the SNRs corresponding to hypotheses H_0 and H_1 , defined in (7), are equal. For large L and SNR, the difference between P_D of the RPT detector in (28) and the hypothetical detector (which corresponds to the PMB) in (29) is well-approximated by*

$$\text{gap}(L, \text{SNR}) = P_D - P_{D_{\text{PMB}}} \approx \frac{e^{-\frac{L \cdot \text{SNR}}{2}} \left(\sqrt{2} - e^{-\frac{L \cdot \text{SNR}}{2}} \right)}{2\sqrt{\pi}\sqrt{L \cdot \text{SNR}}}. \quad (31)$$

Accordingly,

$$\lim_{L \cdot \text{SNR} \rightarrow \infty} \frac{|\log \text{gap}|}{L \cdot \text{SNR}} = O(1), \quad (32)$$

where $O(1)$ is a constant¹.

¹This is the standard Big O notation, so that $f(x) = O(g(x))$ iff there exists positive numbers C and x_0 such that $|f(x)| \leq Cg(x), \forall x \geq x_0$.

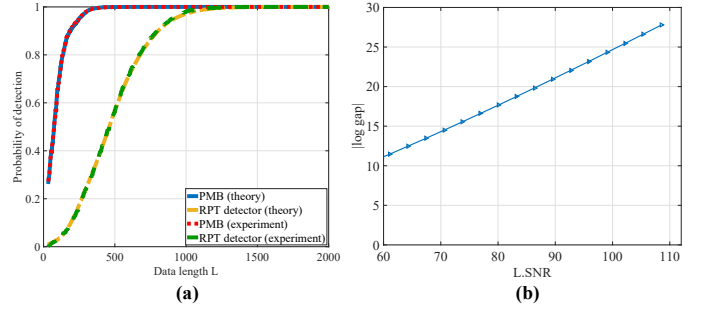


Fig. 4. (a) PMB and P_D of the binary RPT detector from both theory and numerical experiment. (b) $|\log \text{gap}|$ scales linearly in $L \cdot \text{SNR}$.

Proof. See Appendix C \square

Lemma 3 indicates that, asymptotically the gap is dominated by the exponentially decaying function, establishing the asymptotic optimality of the proposed RPT detector, in the sense that the performance gap with respect to the PMB – which provides an upper bound on the performance of any composite test – approaches zero.

For a numerical example, we consider (7) and assume that the periods corresponding to the two stimuli are $T_0 = 32$ and $T_1 = 18$ under hypotheses H_0 and H_1 , respectively. We fix $\text{SNR} = -15\text{dB}$ and generate 5000 observation vectors \mathbf{y} under each hypothesis. Fig. 4(a) depicts the difference between the PMB and P_D for the RPT detector in (14) as we vary L from $\max\{T_0, T_1\}$ to 2000. The figure confirms that the numerical experiments are in agreement with the analytical Gaussian approximations and verifies the asymptotic optimality of the RPT detector. The constant slope of Fig. 4(b) corroborates the linear scaling of $|\log \text{gap}|$ with respect to the product $L \cdot \text{SNR}$ as we derived in (32).

C. Multi-class and Multi-electrode SSVEP Detection

1) *Composite M-ary hypothesis testing model:* Our model in (7) can be extended to distinguishing $M > 2$ hypotheses (multiple classes) H_m corresponding to M stimuli and periodic brain responses with frequencies $f_m, m \in \mathcal{M} = \{0, 1, \dots, M-1\}$. We can also take into account the measurements collected (recorded) from multiple electrodes. Since these electrodes lie in close proximity, their signals are not independent. Hence, it is important that such an extended model also captures the spatial correlation between the measurements of different electrodes. We extend the model in (7) to M hypotheses, in which the measurements under each hypothesis are modeled as

$$\begin{aligned} H_0 : \mathbf{Y} &= \mathbf{K}\mathbf{X}_0 + \mathbf{W} \\ H_1 : \mathbf{Y} &= \mathbf{K}\mathbf{X}_1 + \mathbf{W} \\ &\vdots \\ H_{M-1} : \mathbf{Y} &= \mathbf{K}\mathbf{X}_{M-1} + \mathbf{W} \end{aligned} \quad (33)$$

where \mathbf{Y} is an $L \times N_c$ observation (measurement) matrix, L is the length of the recorded data, N_c is the number of electrodes (channels), and $\mathbf{X}_m, m \in \mathcal{M}$ are the signal representations of the observations in the RPT subspace. Similar to the composite binary hypothesis testing model in Section II-B, the signal representations $\mathbf{X}_m, m \in \mathcal{M}$, are modeled as M deterministic

$$P_D = Q \left(\frac{Q^{-1}(\alpha) \sqrt{2(r_B + r_A) + 4(\lambda_{0,A}^2 - \lambda_{0,B}^2) - 4 \sum_{i=1}^L \sum_{j=1}^L c_{ij} + \lambda_{0,B}^2 + \lambda_{1,A}^2 - \lambda_{0,A}^2 - \lambda_{1,B}^2}}{\sqrt{(2(r_B + r_A) + 4(\lambda_{1,B}^2 - \lambda_{1,A}^2) - 4 \sum_{i=1}^L \sum_{j=1}^L c_{ij})}} \right) \quad (28)$$

$$P_{D_{\text{PMB}}} = Q \left(Q^{-1}(\alpha) - \sqrt{\mathbf{x}_{S_1}^T \mathbf{K}_{S_1}^T \mathbf{K}_{S_1} \mathbf{x}_{S_1} + \mathbf{x}_{S_0}^T \mathbf{K}_{S_0}^T \mathbf{K}_{S_0} \mathbf{x}_{S_0} - \mathbf{x}_{S_1}^T \mathbf{K}_{S_1}^T \mathbf{K}_{S_0} \mathbf{x}_{S_0} - \mathbf{x}_{S_0}^T \mathbf{K}_{S_0}^T \mathbf{K}_{S_1} \mathbf{x}_{S_1}} \right) \quad (29)$$

but unknown matrices and we restrict the row support of the signal representation \mathbf{X}_m under the m -th hypothesis to the atoms of the RPT dictionary matrix \mathbf{K} that span the subspace of periodic signals with period T_m . We denote the known support sets $\text{supp}(\mathbf{X}_m)$ for \mathbf{X}_m by $S_m := \{j : \mathbf{x}_{m,j} \neq \mathbf{0}\}$, where $\mathbf{x}_{m,j}$ is the j -th row of \mathbf{X}_m , $m = 0, \dots, M-1$. Let $\mathbf{y}_l, \mathbf{k}_l$ and \mathbf{w}_l denote the l -th row of \mathbf{Y}, \mathbf{K} and \mathbf{W} , respectively. From the extended model in (33) we have

$$\mathbf{y}_l = \mathbf{k}_l \mathbf{X}_m + \mathbf{w}_l, \quad l = 1, \dots, L, \quad m \in \mathcal{M}. \quad (34)$$

The noise vector \mathbf{w}_l is assumed to be Gaussian with covariance matrix $\Sigma_{\mathbf{w}}$, i.e., $\mathbf{w}_l \sim \mathcal{N}(\mathbf{0}, \Sigma_{\mathbf{w}})$, where $\Sigma_{\mathbf{w}}$ captures the spatial correlation between the measurements of different electrodes. Under these assumptions, we have $\mathbf{y}_l \sim \mathcal{N}(\mathbf{k}_l \mathbf{X}_m, \Sigma_{\mathbf{w}})$. Also, we assume the vectors $\mathbf{w}_l, l = 1, \dots, L$, are independent and identically distributed.

2) *Multi-class RPT detector*: Let $f(\mathbf{Y}|H_m)$ denote the conditional pdf of the measurement matrix \mathbf{Y} given hypothesis H_m . For the extended model in (33) we can write:

$$f(\mathbf{Y}|H_m) = \prod_{l=1}^L \frac{1}{(2\pi)^{\frac{N_c}{2}} |\Sigma_{\mathbf{w}}|^{\frac{1}{2}}} \exp\left(-\frac{(\mathbf{y}_l - \mathbf{k}_l \mathbf{X}_m) \Sigma_{\mathbf{w}}^{-1} (\mathbf{y}_l - \mathbf{k}_l \mathbf{X}_m)^T}{2}\right). \quad (35)$$

Similar to the binary RPT detector in Section II-B, the multi-class RPT detector is obtained from the GLRT assuming uniform prior probabilities $P(H_m) = \frac{1}{M}$ and uniform cost assignment [28]. We define the generalized likelihood ratios (GLRs)

$$\mathcal{L}_m(\mathbf{Y}) \triangleq \frac{\max_{\mathbf{X}_m: \text{supp}(\mathbf{X}_m)=S_m} f(\mathbf{Y}|H_m)}{\max_{\mathbf{X}_0: \text{supp}(\mathbf{X}_0)=S_0} f(\mathbf{Y}|H_0)}, \quad m = 1, \dots, M-1, \quad (36)$$

which require computing the restricted ML estimate of \mathbf{X}_m when the support set is restricted to S_m for $m \in \mathcal{M}$. Let $\hat{\mathbf{X}}_m$ denote the ML estimate of \mathbf{X}_m when the row support set is restricted to S_m . From (35), we find that the ML estimate $\hat{\mathbf{X}}_m$ is the solution to the following

$$\min_{\mathbf{X}_m: \text{supp}(\mathbf{X}_m)=S_m} \text{tr} \left((\mathbf{Y} - \mathbf{K} \mathbf{X}_m) \Sigma_{\mathbf{w}}^{-1} (\mathbf{Y} - \mathbf{K} \mathbf{X}_m)^T \right) \quad (37)$$

such that $\mathbf{x}_{m,j} = \mathbf{0}, \forall j \in S_m^c$. Accordingly, (37) can be rewritten as

$$\min \text{tr} \left((\mathbf{Y} - \mathbf{K}_{S_m} \mathbf{X}_{S_m}) \Sigma_{\mathbf{w}}^{-1} (\mathbf{Y} - \mathbf{K}_{S_m} \mathbf{X}_{S_m})^T \right) \quad (38)$$

where \mathbf{K}_{S_m} and \mathbf{X}_{S_m} are the columns of \mathbf{K} and rows of \mathbf{X}_m indexed by S_m , respectively. The solution to (38) can be written as (for proof see Appendix D)

$$\hat{\mathbf{X}}_{S_m} = (\mathbf{K}_{S_m}^T \mathbf{K}_{S_m})^{-1} \mathbf{K}_{S_m}^T \mathbf{Y}. \quad (39)$$

Thus, the decision \hat{m} is obtained by replacing (35) in (36), which gives

$$\hat{m}(\mathbf{Y}) = \arg \max_{m \in \mathcal{M}} \text{tr} \left(\mathbf{Y} \Sigma_{\mathbf{w}}^{-1} \hat{\mathbf{X}}_{S_m}^T \mathbf{K}_{S_m}^T - \frac{\mathbf{K}_{S_m} \hat{\mathbf{X}}_{S_m} \Sigma_{\mathbf{w}}^{-1} \hat{\mathbf{X}}_{S_m}^T \mathbf{K}_{S_m}^T}{2} \right). \quad (40)$$

Replacing with the estimates in (39), we reach

$$\hat{m}(\mathbf{Y}) = \arg \max_{m \in \mathcal{M}} \text{tr} (\mathbf{Y} \Sigma_{\mathbf{w}}^{-1} \mathbf{Y}^T \mathbf{A}_m), \quad (41)$$

where \mathbf{A}_m is

$$\mathbf{A}_m = \mathbf{K}_{S_m} (\mathbf{K}_{S_m}^T \mathbf{K}_{S_m})^{-1} \mathbf{K}_{S_m}^T. \quad (42)$$

D. Error Exponent - Discrimination Rate Tradeoff

It is conceivable that a reliable detection scheme should be able to leverage on information obtained from additional electrodes to boost the system's efficiency, given that the detector is tasked with distinguishing between a fixed number of classes. Alternatively, for the same efficiency, the additional electrodes may be exploited to increase the detector's ability to discriminate a larger number of classes. This insight is the basis for a new tradeoff, introduced here for the first time in the context of SSVEP detection, between 'error exponent' and the 'discrimination rate' defined in our problem setup as $-\log P_e / (L \cdot \text{SNR})$ and $\log_2 M$, respectively. Inspired by the notion of diversity and multiplexing tradeoff in information theory [23], our goal is to provide a suitable metric associated with a broader spectrum of operating regimes across which different SSVEP detection methods could be compared. Specifically, given the system resources L and SNR, a detection method can leverage a multi-electrode EEG system (with N_c electrodes) to trade the system's efficiency (measured by the error probability P_e associated with the detector) for a higher discrimination rate (the detector's ability to discriminate M classes, measured by $\log_2 M$) and vice-versa. The error probability P_e in the binary hypothesis testing setting with uniform prior probabilities $P(H_0) = P(H_1) = 1/2$ is $P_e = \frac{1}{2}(1 - P_D + P_F)$, thus it can be approximated in the high SNR regime as

$$P_e = \frac{e^{-\frac{L \cdot \text{SNR}}{8}}}{\sqrt{2\pi} \sqrt{L \cdot \text{SNR}/4}}, \quad (43)$$

using the expressions of P_D and P_F derived in (27) and the Q-function approximation. Since $-\log P_e/(L \cdot \text{SNR})$ captures the rate at which the error probability decays with L and SNR, we use the logarithm of the error probability as a measure of the system's efficiency. For distinguishing between M classes, we define the average error probability as

$$P_e = \frac{1}{M} \sum_{m=1}^M P(H_j|H_m) \quad \text{for } j \neq m. \quad (44)$$

As a result, we can characterize the error probability for an entire spectrum of regimes corresponding to different discrimination rates for a given number of electrodes N_c and system resources (in terms of data length L and SNR).

III. NUMERICAL RESULTS

In this section, we start off by presenting some numerical results from experiments with synthesized data to verify and validate the theory developed for the binary RPT detector of Section II-B. Then, we provide results for the multi-class and multi-electrode RPT detector using both synthesized and real data, along with comparisons to the existing SSVEP detection methods, including PSDA, standard CCA and IT CCA [9]. As real data, we employ a publicly available SSVEP dataset [11], which contains multiple goal frequencies (frequencies of stimuli) $f_m, m = 0, \dots, M - 1$, with a sampling frequency of $f_s = 256$ Hz, and M is the number of classes to be discriminated. The data length L (measured in samples) is related to the data length T (measured in seconds) through $T = L/f_s$. We study the classification accuracy $A = 1 - P_e$ and the Information Transfer Rate (ITR) defined in [11] in terms of the number of classes to be discriminated M , the classification accuracy A , and the data length T in seconds,

$$\text{ITR} = \left(\log_2 M + A \log_2 A + (1 - A) \log_2 \left(\frac{1 - A}{M - 1} \right) \right) \left(\frac{60}{T} \right).$$

We further discuss the advantage of NPMs as finite complete bases for estimating the periods of periodic sequences and study the newly introduced error exponent-discrimination rate tradeoff in terms of the number of electrodes N_c .

A. Theoretical Validation of Binary RPT Detector Using Synthesized Data

Fig. 3 validated our theoretical results for the binary RPT detector for the orthogonal case when $L = \text{lcm}(T_0, T_1)$. Here, we validate our theoretical results for the general case when L is arbitrary. We consider (7) and fix $\text{SNR} = -15$ dB and generate 2500 observation vectors \mathbf{y} under each hypothesis. We consider two cases: for case (a) we assume that the periods corresponding to the two stimuli are $T_0 = 15$ and $T_1 = 25$ under hypotheses H_0 and H_1 , respectively, and for case (b) we assume $T_0 = 32$ and $T_1 = 18$. Fig. 5 illustrates the ROC curves for these two cases, where P_D and P_F are obtained using both the expressions derived in (27) and the numerical experiment. Fig. 6(a) and Fig. 6(b) show the error probability P_e , and the classification accuracy A in terms of the data length L for the setup in case (b). These two figures show that results from both theory and experiments strongly agree.

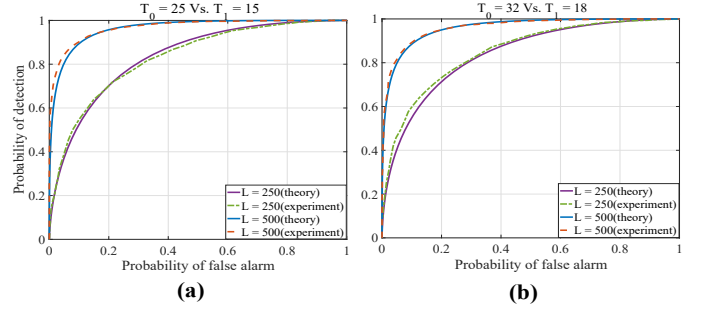


Fig. 5. ROC curves show P_D versus P_F for both theory (Gaussian approximated pdfs) and numerical experiment. (a) $T_0 = 25, T_1 = 15$, (b) $T_0 = 32, T_1 = 18$.

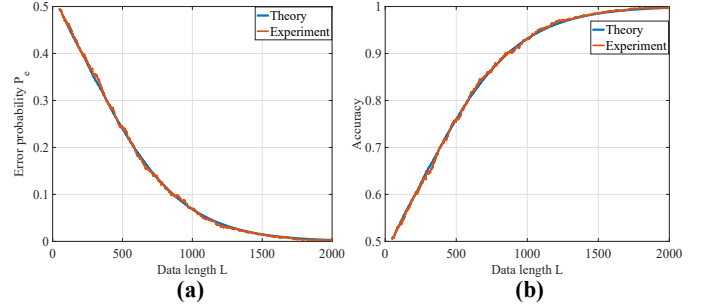


Fig. 6. $T_0 = 32$ and $T_1 = 18$ (a) error Probability P_e is obtained using both theory (Gaussian approximated pdfs) and numerical experiment. (b) Classification accuracy versus data length L (in number of samples).

B. Real Data Description for Validation of Multi-class and Multi-electrode RPT Detector

The public SSVEP dataset [11] we use is generated based on the sampling frequency of $f_s = 256$ Hz. Ten subjects have participated in the experiment and 15 trials have been recorded for each subject per goal frequency. Hence, the dataset has a total number of 150 trials for each goal frequency. We use 9 goal frequencies (i.e., the number of classes to be discriminated is $M = 9$) for performance validation of the RPT detector and performance comparison among different SSVEP detection methods. These 9 goal frequencies are $f_0 = 9.25, f_1 = 9.75, f_2 = 10.25, f_3 = 10.75, f_4 = 11.25, f_5 = 11.75, f_6 = 12.25, f_7 = 12.75$ and $f_8 = 14.25$ Hz. All the recorded data is filtered using 4-30 Hz bandpass filters. The trials are recorded using 8 electrodes positioned on the occipital region of the subject's brain cortex as depicted in Fig. 7. The period T_m corresponding to each goal frequency f_m is computed as $T_m = f_s/f_m$, then is rounded to its nearest integer value.

C. Validation of Multi-class and Multi-electrode RPT Detector Using Synthesized and Real Data

In this section, we investigate the performance of the multi-class and multi-electrode RPT detector obtained in (41). Since all the electrodes are located on the occipital region of the brain cortex, the collected data is normally correlated. As described in Section II-C, our model captures the spatial correlation between the data of different electrodes through the covariance matrix $\Sigma_{\mathbf{w}}$. We use *pre-stimulus* data to find a sample covariance matrix and use it as an estimate of the true $\Sigma_{\mathbf{w}}$. An advantage of using only pre-stimulus data segments in estimating $\Sigma_{\mathbf{w}}$ is that one does not need to collect data

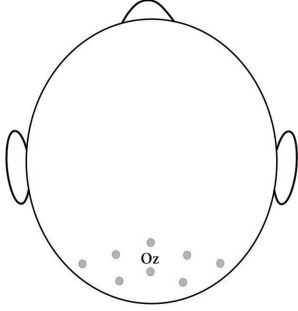


Fig. 7. Eight electrodes are positioned on the occipital region of the subject’s brain cortex.

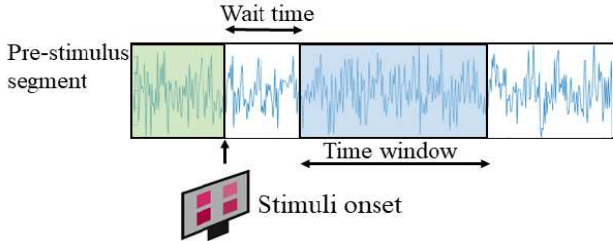


Fig. 8. Schematic for an SSVEP observation. There is an unknown latency between the stimulus onset and the brain’s response.

from each subject under each goal frequency f_m . This is important in practice as it significantly reduces the time, cost, and overhead associated with data collection, especially with a large number of classes and subjects.

•*Latency and its effect on the performances of SSVEP detection methods:* It is well recognized that there exists a delay (latency) between the onset of an external stimulus and the beginning of the brain’s response [10]. This delay widely varies among different subjects and is generally unknown. The latency is an important factor that affects the performance of all SSVEP detection methods. To test the performance of the RPT detector with respect to this uncontrolled latency, we define Wait time and Time window (See Fig. 8). Wait time is the time between the stimulus onset and the beginning of Time window. Time window is the portion of the recorded data we are using for our performance evaluation with length

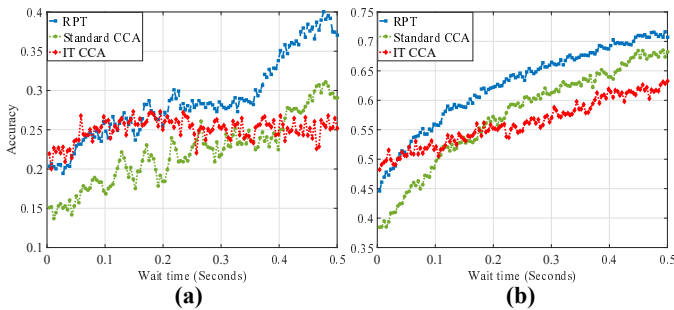


Fig. 9. Classification accuracy with (a) 0.5 second post-stimulus SSVEPs and (b) 1 second post-stimulus SSVEPs. The wait time represents the time between the onset of the stimulus and the beginning of our time window intended to capture the time it takes for the brain to respond to the external stimulus.

T measured in seconds. Fig. 9(a) and Fig. 9(b) compare the performance of the RPT detector to those of standard CCA and IT CCA using 0.5 second and 1 second of post-stimulus data as the wait time varies, respectively. Fig. 9 demonstrates that the performance of all methods improve as we increase the wait time due to an improved SNR. Noting that the computational complexity and performance of all these methods depend on the data length underscores an important advantage of the RPT approach. In particular, taking the latency into account one could attain a better performance for a short data length which is crucial for real-time BCI. As shown, for the short data lengths used, the RPT method achieves higher accuracy. Based on these results we consider a 0.25 second wait time after the onset of the stimulus.

•*Effect of spatial correlation knowledge on the RPT detector performance:* Fig. 10(a) presents the classification accuracy A as function of the data length T for a multi-class multi-electrode RPT detector using synthesized data. In this experiment, we generate periodic sequences with $N_c = 8$ electrodes for $M = 9$ classes. The dashed blue curve corresponds to a genie-aided RPT detector that knows Σ_w . The dotted red curve is obtained when the RPT detector uses an estimate of Σ_w obtained from pre-stimulus data (real recorded data from one of the subjects). The dashed green curve is for a RPT detector that falsely assumes no spatial correlation between the recorded data from different electrodes and classifies the data thereof, hence this case is denoted as ‘model mismatch’.

•*Performance comparison of different SSVEP methods using real data:* Figs. 10(b) and 10(c) illustrate the accuracy and ITR of an RPT detector with $N_c = 8$ electrodes and $M = 9$ classes. This result is obtained using leave-p-out cross validation for $p = 12$, which indicates that only 20% of the data is used for training. Note that IT CCA outperforms other methods if we increase the number of training trials for each class. Fig. 11 shows the accuracy and ITR of the aforementioned methods for a multi-class multi-electrode setting using leave-one-out cross validation (i.e., we use the maximum number of training trials to construct the reference matrix. The reference matrix is defined later). While IT CCA achieves the highest performance, it is important to note that it requires post-stimulus trials to construct the reference matrix. Hence, IT CCA boosts the performance of standard CCA at the expense of additional training with post-stimulus data per subject. By contrast, the RPT detector is unsupervised, in the sense that it only uses training to estimate the spatial correlation matrix Σ_w per subject from pre-stimulus data. Our results also indicate that the RPT detector can outperform PSDA and standard CCA methods for short data lengths, i.e., less than 1.5 seconds.

D. Difference between Standard CCA and RPT Detection Methods From Basis Representation Perspective

In this section, we clarify a fundamental difference between standard CCA and the proposed RPT method and that is the completeness of the basis used for signal representation. Standard CCA first constructs a reference matrix $\mathbf{Q}_m \in \mathbb{R}^{2N_h \times L}$

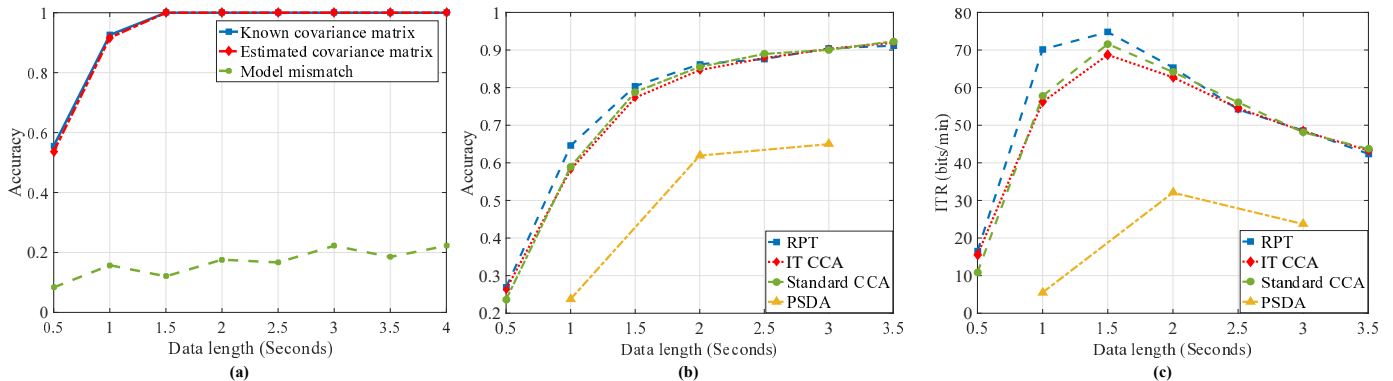


Fig. 10. Number of classes and electrodes are $M = 9$ and $N_c = 8$, (a) Classification accuracy A versus the data length T , synthesized data is used to generate the plots, they compare A when the RPT detector knows the true Σ_w (dashed blue), Σ_w is unknown and the RPT detector estimates Σ_w using pre-stimulus data (dotted red), the RPT detector falsely assumes there is no spatial correlation between recorded data of different electrodes (dashed green) (b) Classification accuracy A versus the data length T , real data is used to generate these plots, they compare the RPT detector, IT CCA, standard CCA, and PSDA. For the PSDA method, the data recorded by the best electrode (the one which yields the highest accuracy) is selected. (c) ITR versus the data length T , real data is used to generate these plots.

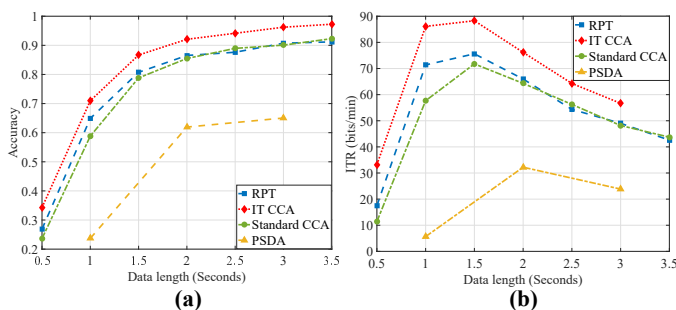


Fig. 11. (a) Classification accuracy and (b) ITR of the RPT detector, IT CCA, standard CCA and PSDA methods using leave-one-out cross validation.

from N_h harmonics. Let $\mathbf{Q}_m = [\mathbf{q}_{m1} \ \dots \ \mathbf{q}_{mL}]$, where \mathbf{q}_{mi} is a $2N_h \times 1$ column vector, defined as

$$\mathbf{q}_{mi} = \left[\sin \frac{\omega_m l}{f_s} \ \cos \frac{\omega_m l}{f_s} \ \dots \ \sin \frac{N_h \omega_m l}{f_s} \ \cos \frac{N_h \omega_m l}{f_s} \right]^T \quad (45)$$

where $\omega_m = 2\pi f_m$ and $l = 1, 2, \dots, L$. For the measurement matrix \mathbf{Y} and the reference matrix \mathbf{Q}_m , standard CCA finds weight vectors \mathbf{w}_y ($N_c \times 1$) and \mathbf{w}_{q_m} ($2N_h \times 1$), which maximize the correlation between linear combinations of the signals recorded from the electrodes $\mathbf{z} = \mathbf{Y}\mathbf{w}_y$ and signals in the reference matrix $\mathbf{s}_m = \mathbf{Q}_m^T \mathbf{w}_{q_m}$ (both are $L \times 1$ vectors) via solving the following optimization problem

$$\rho_m = \max \rho(\mathbf{z}, \mathbf{s}_m) = \max_{\mathbf{w}_y, \mathbf{w}_{q_m}} \frac{\mathbb{E}[\mathbf{z}\mathbf{s}_m^T]}{\sqrt{\mathbb{E}[\mathbf{z}\mathbf{z}^T]\mathbb{E}[\mathbf{s}_m\mathbf{s}_m^T]}}, \quad (46)$$

where ρ_m is known as the maximum canonical correlation. Solving the optimization problem in (46) M times, once for each goal frequency f_m , and finding ρ_m 's, standard CCA obtains the decision using the following rule

$$\hat{m} = \arg \max_{m \in \mathcal{M}} \{\rho_0, \dots, \rho_{M-1}\}. \quad (47)$$

However, such reference matrices do not form a finite complete basis for representing periodic signals. Hence, to be able to represent fully periodic signal, Standard CCA requires an infinite number of harmonics to construct \mathbf{Q}_m matrices. Therefore, the performance of Standard CCA depends on the number of harmonics used in the reference matrix. By contrast, in the RPT method we leverage a complete finite basis in the form of NPMs. To demonstrate this fact using

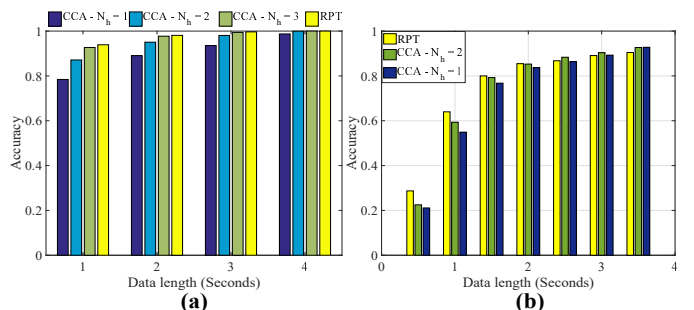


Fig. 12. (a) Classification accuracy of standard CCA and the RPT detector on synthesized data, (b) real data.

synthesized data, we generate random periodic sequences with periods $T_0 = 32$ and $T_1 = 18$ that correspond to the two stimuli under hypotheses H_0 and H_1 , respectively. We fix $\text{SNR} = -12$ dB and generate 2000 observation vectors \mathbf{y} under each hypothesis. Fig. 12(a) depicts the classification accuracy of the binary RPT detector and standard CCA versus different data lengths T using the generated data. For the standard CCA method we consider three cases: in the first case we let the number of harmonics $N_h = 1$ to generate the \mathbf{Q}_m reference matrices, in the second case $N_h = 2$, and in the third case $N_h = 3$. To produce Fig. 12(b) we use the real data, and for standard CCA we consider two cases of $N_h = 1$ and $N_h = 2$. Both figures show that the accuracy of standard CCA method improves as we increase N_h and enrich the reference matrices. This is in contrast to the RPT detection method which uses a finite complete basis for representing the periodic signals.

E. Error Exponent- Discrimination Rate Tradeoff Based on Real and Synthesized Data

In this section, we show the error exponent-discrimination rate tradeoff using both synthesized and real data.

•*Tradeoff based on synthesized data:* We generate random periodic sequences with period $T_m = T_0 + (m - 1)\Delta T$, where $T_0 = 10$ and $\Delta T = 1$ under the model in (33) for $M = 11$ classes and $N_c = 8$ electrodes. We fix the data length $L = 50$ samples and $\text{SNR} = -10$ dB and we generate 500 observations under each hypothesis. We let the (i, j) -th entry of the spatial correlation matrix be $\Sigma_{\mathbf{w}i,j} = \rho^{d_{ij}}$

for some $0 < \rho < 1$, where d_{ij} denotes the distance between electrodes i and j . Fig. 13(a) and 13(b) plot the error exponent $-\log P_e/(L \cdot \text{SNR})$ versus the discrimination rate $\log_2 M$ using the generated synthesized data for $N_c = 4$ and $N_c = 8$, respectively. These figures show that the RPT detector achieves a better tradeoff compared to standard CCA. Fig. 13(c) plots the same using the synthesized data for the RPT detector for $N_c = 1, 2, 4, 8$. This figure shows that a larger N_c yields a better tradeoff between the error exponent and the discrimination rate.

•*Tradeoff based on real data:* Fig. 14(a) illustrates the tradeoff using real data for $L = 256$ ($T = 1$ second) and $N_c = 8$, indicating that the RPT detector exhibits a better tradeoff compared to standard CCA and IT CCA methods. Fig. 14(b) plots the same using real data for the RPT detector for $N_c = 1, 2, 4, 8$, verifying that a larger N_c provides a better tradeoff between the error exponent and the discrimination rate. In these experiments SNR is estimated from pre-stimulus and post-stimulus data.

IV. DISCUSSION

We started with an in depth analysis of a composite binary hypothesis testing framework to detect periodic SSVEP responses. The RPT detector distinguishes M classes (corresponding to M hypotheses H_m) using the Ramanujan subspace, i.e., the RPT detector chooses the class corresponding to the subspace that yields the largest projection. We remark that NPMs are designed for integer periodicity estimation. Hence, we have to round the periods corresponding to the stimuli frequencies to the nearest integer values. This is the main drawback of employing the RPT detector for SSVEP detection since we may not have exact integer periods. Given the model in section II-C1, the Ramanujan matrix \mathbf{K}_{S_m} corresponding to T_m contains the submatrices \mathbf{R}_m and $\mathbf{R}_{d|m}$. Therefore, the submatrices within, inherently span the subspace of T_m and its divisors. If T_m is an even integer, its divisors correspond to even harmonics of the goal frequency f_m (i.e., nf_m where n is even), which can enhance the performance of the RPT detector.

We also compared the performance of the RPT detector to that of a fictitious detector that knows \mathbf{x}_0 and \mathbf{x}_1 , i.e., the signal representations in the RPT dictionary. This detector yields an upper bound on the performance for the composite test. As shown in Fig. 4, the RPT detector based on the GLRT is asymptotically optimal as it closes the gap to the perfect measurement bound as L increases.

The proposed RPT detection method is unsupervised since it does not use any information from post-stimulus data and uses only pre-stimulus data to estimate the covariance matrix capturing the spatial correlation between the recorded data of different electrodes. The performance of supervised methods is heavily dependent on the number of training trials. For instance, for the IT CCA method it is crucial to have enough training data to construct the reference matrices and it has been shown that reducing the number of training trials can deteriorate the performance of the method.

In contrast to the reference matrix in standard CCA which does not provide a complete basis for periodic signals, the

RPT detector leverages a complete dictionary spanning the subspaces of all periodic signals.

V. CONCLUSION

We proposed and analyzed a new approach to SSVEP detection using linear representations in RPT dictionaries known to be robust to noise and latency. The RPT detector outperforms the state-of-the-art methods in the short data length regime crucial for real-time BCI. Further, it does not depend on post-stimulus data, which reduces the overhead associated with data collection in supervised methods. Furthermore, we introduced a new tradeoff between the error exponent and the discrimination rate, which can serve as a basis for comparing SSVEP detection schemes across an entire range of operation regimes where efficiency is traded for rate and vice-versa.

APPENDIX A

PROOF OF THEOREM 2

From [29, Lemma 1.1], the RVs $\mathbf{y}^T \mathbf{B}^\perp \mathbf{y}$ and $\mathbf{y}^T \mathbf{A}^\perp \mathbf{y}$ in (15) have non-central Chi-squared distributions with r_B^\perp and r_A^\perp degrees of freedom and non-centrality parameters $\lambda_{m,B}^{2,\perp}$ and $\lambda_{m,A}^{2,\perp}$, respectively, under hypothesis H_m , where $r_B^\perp = \text{tr}(\mathbf{B}^\perp)$, $r_A^\perp = \text{tr}(\mathbf{A}^\perp)$, $\lambda_{m,B}^{2,\perp} = \boldsymbol{\mu}_m^T \mathbf{B}^\perp \boldsymbol{\mu}_m$, $\lambda_{m,A}^{2,\perp} = \boldsymbol{\mu}_m^T \mathbf{A}^\perp \boldsymbol{\mu}_m$ and $\boldsymbol{\mu}_m$ is the mean of the observation \mathbf{y} under H_m . Moreover, we have shown in Lemma 1 that $\mathbf{A}^\perp \mathbf{B}^\perp = \mathbf{0}$. Hence, it follows from [31] that $\mathbf{y}^T \mathbf{B}^\perp \mathbf{y}$ and $\mathbf{y}^T \mathbf{A}^\perp \mathbf{y}$ are independent. From the definitions above and the orthogonality of the submatrices associated with different divisors, we can readily show that $\lambda_{1,A}^{2,\perp} = \lambda_{0,B}^{2,\perp} = 0$. Therefore, the test statistic $\ell(\mathbf{y})$ in (15) is the difference between a non-central and a central Chi-squared RV. Per [32, Theorem 1.1], a non-central Chi-squared RV with n degrees of freedom can be represented as a sum of a non-central Chi-squared RV with one degree of freedom with the same non-centrality parameter and a central Chi-squared RV with $n - 1$ degrees of freedom. Moreover, we can write a central Chi-squared RV with $(m + n)$ degrees of freedom as the sum of two independent Chi-squared RVs with m and n degrees of freedom. Accordingly, under H_1 ,

$$\ell(\mathbf{y}) = \ell_1(\mathbf{y}) + \ell_2(\mathbf{y}) - \ell_3(\mathbf{y}) - \ell_4(\mathbf{y}) \quad (48)$$

where $\ell_1(\mathbf{y}) \sim \chi^2(1, \lambda_{1,B}^{2,\perp})$, $\ell_2(\mathbf{y}) \sim \chi^2(r_B^\perp - 1, 0)$, $\ell_3(\mathbf{y}) \sim \chi^2(1, 0)$ and $\ell_4(\mathbf{y}) \sim \chi^2(r_A^\perp - 1, 0)$. Using [30, Theorem 3.3] which characterizes the distribution of the difference of linear combinations of non-central Chi-squared RVs, we can express the distribution of $\ell(\mathbf{y})$ as

$$h(t) = \sum_{i=0}^{\infty} \sum_{j=0}^{\infty} q_i l_j p_{r_B^\perp + 2i, r_A^\perp + 2j}(t), \quad (49)$$

where $p_{a,b}(\cdot)$ is defined in (18), and following from [30, Theorem 2.1A] and (48), we can readily obtain the coefficients q_i 's and l_j 's as

$$q_0 = \exp\left(\frac{-\lambda_{1,B}^{2,\perp}}{2}\right), \quad l_0 = 1, \quad (50)$$

$$q_i = \frac{\exp\left(\frac{-\lambda_{1,B}^{2,\perp}}{2}\right) \left(\frac{\lambda_{1,B}^{2,\perp}}{2}\right)^i}{i!} \quad \text{for } i \neq 0, \quad (51)$$

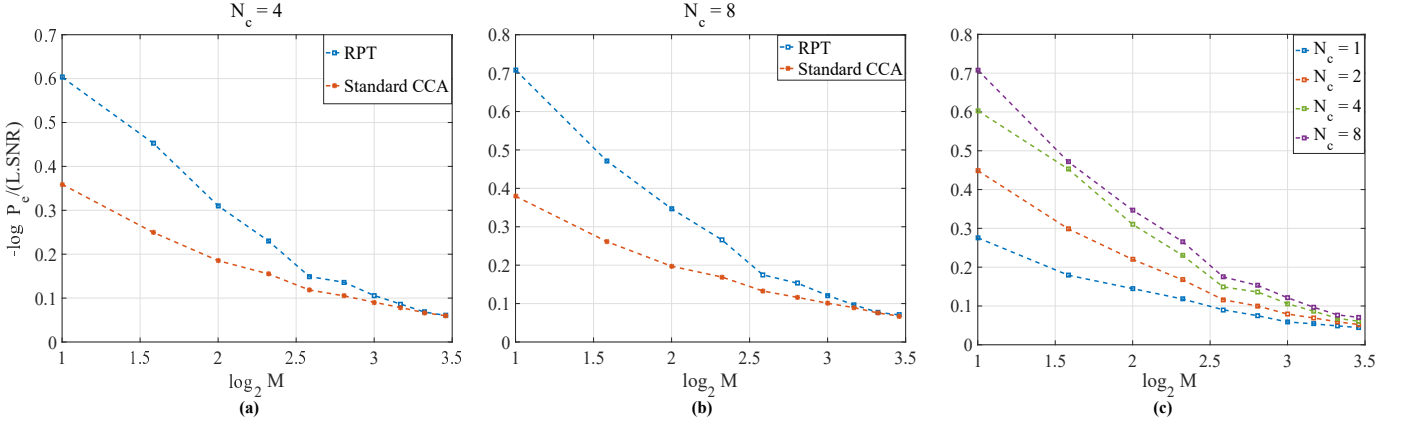


Fig. 13. (a) and (b) Error exponent-discrimination rate tradeoff using synthesized data for $N_c = 4$ and $N_c = 8$ respectively, with M changing from 2 to 11 with fixed $L = 50$ and $\text{SNR} = -10$ dB. (c) Error exponent-discrimination rate tradeoff for the RPT detector using synthesized data for different N_c .

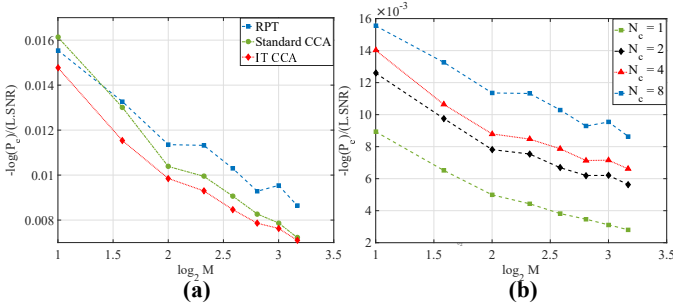


Fig. 14. (a) Error exponent-discrimination rate tradeoff using real data with M changing from 2 to 9 with fixed $L = 256$ and $N_c = 8$. (b) Error exponent-discrimination rate tradeoff of the RPT detector for different N_c .

and $l_j = 0$ for $j > 0$. Similarly, we can derive the corresponding coefficients under H_0 . Based on the aforementioned definitions for the non-centrality parameters, we have

$$\begin{aligned}\lambda_{0,A}^{2,\perp} &= \mathbf{x}_{S_0}^T \mathbf{K}_{S_0}^T \mathbf{A}^\perp \mathbf{K}_{S_0} \mathbf{x}_{S_0} \\ \lambda_{1,B}^{2,\perp} &= \mathbf{x}_{S_1}^T \mathbf{K}_{S_1}^T \mathbf{B}^\perp \mathbf{K}_{S_1} \mathbf{x}_{S_1}\end{aligned}\quad (52)$$

which subsequently leads to the equations in (20).

APPENDIX B PROOF OF (26)

Here, we analyze the covariance of the two quadratic terms in the expression of the test statistic $\ell(\mathbf{y})$ in (14) under H_0 .

$$\begin{aligned}\text{Cov}(\mathbf{y}^T \mathbf{B} \mathbf{y}, \mathbf{y}^T \mathbf{A} \mathbf{y} | H_0) \\ = \mathbb{E}_0[\mathbf{y}^T \mathbf{B} \mathbf{y} \mathbf{y}^T \mathbf{A} \mathbf{y}] - \mathbb{E}_0[\mathbf{y}^T \mathbf{B} \mathbf{y}] \mathbb{E}_0[\mathbf{y}^T \mathbf{A} \mathbf{y}]\end{aligned}\quad (53)$$

where \mathbb{E}_m denotes the expectation under H_m . Focusing on the first term in (53) we expand it as below:

$$\begin{aligned}\mathbb{E}_0[\mathbf{y}^T \mathbf{B} \mathbf{y} \mathbf{y}^T \mathbf{A} \mathbf{y}] &= \\ &\mathbf{x}_{S_0}^T \mathbf{K}_{S_0}^T \mathbf{B} \mathbf{K}_{S_0} \mathbf{x}_{S_0} \mathbf{x}_{S_0}^T \mathbf{K}_{S_0}^T \mathbf{A} \mathbf{K}_{S_0} \mathbf{x}_{S_0} + \mathbb{E}[\mathbf{w}^T \mathbf{B} \mathbf{w} \mathbf{w}^T \mathbf{A} \mathbf{w}] \\ &+ \mathbf{x}_{S_0}^T \mathbf{K}_{S_0}^T \mathbf{B} \mathbb{E}[\mathbf{w} \mathbf{x}_{S_0}^T \mathbf{K}_{S_0}^T \mathbf{w}] + \mathbf{x}_{S_0}^T \mathbf{K}_{S_0}^T \mathbf{B} \mathbb{E}[\mathbf{w} \mathbf{w}^T] \mathbf{K}_{S_0} \mathbf{x}_{S_0} \\ &+ \mathbf{x}_{S_0}^T \mathbf{K}_{S_0}^T \mathbf{B} \mathbb{E}[\mathbf{w} \mathbf{w}^T \mathbf{A} \mathbf{w}] + \mathbb{E}[\mathbf{w}^T \mathbf{B} \mathbf{K}_{S_0} \mathbf{x}_{S_0} \mathbf{x}_{S_0}^T \mathbf{K}_{S_0}^T \mathbf{w}] \\ &+ \mathbb{E}[\mathbf{w}^T \mathbf{B} \mathbf{K}_{S_0} \mathbf{x}_{S_0} \mathbf{w}^T] \mathbf{K}_{S_0} \mathbf{x}_{S_0} + \mathbb{E}[\mathbf{w}^T \mathbf{B} \mathbf{K}_{S_0} \mathbf{x}_{S_0} \mathbf{w}^T \mathbf{A} \mathbf{w}] \\ &+ \mathbb{E}[\mathbf{w}^T \mathbf{B} \mathbf{w}] \mathbf{x}_{S_0}^T \mathbf{K}_{S_0}^T \mathbf{A} \mathbf{K}_{S_0} \mathbf{x}_{S_0} + \mathbb{E}[\mathbf{w}^T \mathbf{B} \mathbf{w} \mathbf{x}_{S_0}^T \mathbf{K}_{S_0}^T \mathbf{w}] \\ &+ \mathbb{E}[\mathbf{w}^T \mathbf{B} \mathbf{w} \mathbf{w}^T] \mathbf{K}_{S_0} \mathbf{x}_{S_0} + \mathbf{x}_{S_0}^T \mathbf{K}_{S_0}^T \mathbf{B} \mathbf{K}_{S_0} \mathbf{x}_{S_0} \mathbb{E}[\mathbf{w}^T \mathbf{A} \mathbf{w}]\end{aligned}\quad (54)$$

Using the definitions in (23), it simplifies to

$$\begin{aligned}\mathbb{E}_0[\mathbf{y}^T \mathbf{B} \mathbf{y} \mathbf{y}^T \mathbf{A} \mathbf{y}] &= \lambda_{0,B}^2 \lambda_{0,A}^2 + r_B r_A + 2 \sum_{i=1}^L \sum_{j=1}^L c_{ij} \\ &+ 4 \lambda_{0,B}^2 + r_B \lambda_{0,A}^2 + r_A \lambda_{0,B}^2\end{aligned}\quad (55)$$

where c_{ij} are the entries of the matrix $\mathbf{C} = \mathbf{A} \odot \mathbf{B}$, where \odot denotes the element-wise product. Similarly, we can show that

$$\mathbb{E}_0[\mathbf{y}^T \mathbf{B} \mathbf{y}] \mathbb{E}_0[\mathbf{y}^T \mathbf{A} \mathbf{y}] = (\lambda_{0,B}^2 + r_B)(\lambda_{0,A}^2 + r_A)\quad (56)$$

Substituting (55) and (56) into (53) we find

$$\text{Cov}(\mathbf{y}^T \mathbf{B} \mathbf{y}, \mathbf{y}^T \mathbf{A} \mathbf{y} | H_0) = 2 \sum_{i=1}^L \sum_{j=1}^L c_{ij} + 4 \lambda_{0,B}^2\quad (57)$$

The term $\text{Cov}(\mathbf{y}^T \mathbf{B} \mathbf{y}, \mathbf{y}^T \mathbf{A} \mathbf{y} | H_1)$ can be derived similarly.

APPENDIX C PROOF OF LEMMA 3

From (8) We have

$$L \cdot \text{SNR}_m = \mathbf{x}_{S_m}^T \mathbf{K}_{S_m}^T \mathbf{K}_{S_m} \mathbf{x}_{S_m}.\quad (58)$$

Based on the definitions of $\lambda_{0,A}^2$ and $\lambda_{1,B}^2$ in (23), we have $L \cdot \text{SNR}_0 = \lambda_{0,A}^2$ and $L \cdot \text{SNR}_1 = \lambda_{1,B}^2$. Borrowing the Q-function approximation in [33] given below

$$Q(x) \approx \frac{e^{-x^2/2}}{\sqrt{2\pi} \sqrt{1+x^2}} \quad \text{for } x > 0,\quad (59)$$

we can approximate (28) and (29) for large values of $L \cdot \text{SNR}_m$ as the following

$$P_D \approx 1 - \frac{e^{-\frac{L(\text{SNR}_0 + \text{SNR}_1)^2}{8 \text{SNR}_1}}}{\sqrt{2\pi} \sqrt{\frac{L(\text{SNR}_0 + \text{SNR}_1)^2}{4 \text{SNR}_1}}}\quad (60)$$

and

$$P_{D_{\text{PMB}}} \approx 1 - \frac{e^{-\frac{L(\text{SNR}_0 + \text{SNR}_1)}{2}}}{\sqrt{2\pi} \sqrt{L(\text{SNR}_0 + \text{SNR}_1)}}.\quad (61)$$

Without loss of generality we assume $\text{SNR} = \text{SNR}_0 = \text{SNR}_1$, and thus we have $L \cdot \text{SNR} = L \cdot \text{SNR}_0 = L \cdot \text{SNR}_1$. Using this assumption we can write:

$$P_D \approx 1 - \frac{e^{-\frac{L \cdot \text{SNR}}{2}}}{\sqrt{2\pi} \sqrt{L \cdot \text{SNR}}}\quad (62)$$

and

$$P_{D_{\text{PMB}}} \approx 1 - \frac{e^{-L \cdot \text{SNR}}}{\sqrt{2\pi} \sqrt{2L \cdot \text{SNR}}}. \quad (63)$$

Therefore, the gap is approximated by

$$\begin{aligned} \text{gap}(L, \text{SNR}) &\approx \frac{e^{-\frac{L \cdot \text{SNR}}{2}}}{\sqrt{2\pi} \sqrt{L \cdot \text{SNR}}} - \frac{e^{-L \cdot \text{SNR}}}{\sqrt{2\pi} \sqrt{2L \cdot \text{SNR}}} \\ &= \frac{e^{-\frac{L \cdot \text{SNR}}{2}} \left(\sqrt{2} - e^{-\frac{L \cdot \text{SNR}}{2}} \right)}{2\sqrt{\pi} \sqrt{L \cdot \text{SNR}}} \end{aligned} \quad (64)$$

with the asymptotic order in (32).

APPENDIX D

Let \mathcal{D} denote the first derivative of the expression in (38) with respect to \mathbf{X}_{S_m} . The estimate $\hat{\mathbf{X}}_{S_m}$ can be obtained by setting \mathcal{D} equal to zero. It is easy to verify the following [34],

$$\begin{aligned} \mathcal{D} &= \frac{\partial}{\partial \mathbf{X}_{S_m}} \text{tr} \left(-2\mathbf{Y}\Sigma_{\mathbf{w}}^{-1} \mathbf{X}_{S_m}^T \mathbf{K}_{S_m}^T \right) + \\ &\quad \frac{\partial}{\partial \mathbf{X}_{S_m}} \text{tr} \left(\mathbf{K}_{S_m} \mathbf{X}_{S_m} \Sigma_{\mathbf{w}}^{-1} \mathbf{X}_{S_m}^T \mathbf{K}_{S_m}^T \right) \\ &= -2\mathbf{K}_{S_m}^T \mathbf{Y}\Sigma_{\mathbf{w}}^{-1} + 2\mathbf{K}_{S_m}^T \mathbf{K}_{S_m} \mathbf{X}_{S_m} \Sigma_{\mathbf{w}}^{-1} \end{aligned}$$

Letting \mathcal{D} equal to zero and solving for \mathbf{X}_{S_m} we find

$$\hat{\mathbf{X}}_{S_m} = \left(\mathbf{K}_{S_m}^T \mathbf{K}_{S_m} \right)^{-1} \mathbf{K}_{S_m}^T \mathbf{Y}.$$

ACKNOWLEDGMENTS

This work was supported in part by NSF Grants CCF-1525990, CCF-1552497 and CCF-1341966.

REFERENCES

- [1] Y. Shin, S. Lee, J. Lee, and H.-N. Lee, "Sparse representation-based classification scheme for motor imagery-based brain-computer interface systems," *Journal of neural engineering*, vol. 9, no. 5, p. 056002, 2012.
- [2] P. Saidi, G. K. Atia, A. Paris, and A. Vosoughi, "Motor imagery classification using multiresolution analysis and sparse representation of EEG signals," in *IEEE Global Conference on Signal and Information Processing*, 2015, pp. 815–819.
- [3] A. P. Liavas, G. V. Moustakides, G. Henning, E. Z. Psarakis, and P. Husar, "A periodogram-based method for the detection of steady-state visually evoked potentials," *IEEE Transactions on Biomedical Engineering*, vol. 45, no. 2, pp. 242–248, 1998.
- [4] W. Yijun, W. Ruiping, G. Xiaorong, and G. Shangkai, "Brain-computer interface based on the high-frequency steady-state visual evoked potential," in *Proceedings of the First International Conf. on Neural Interface and Control*, May 2005, pp. 37–39.
- [5] H. Hotelling, "Relations between two sets of variates," *Biometrika*, vol. 28, no. 3/4, pp. 321–377, 1936.
- [6] Z. Lin, C. Zhang, W. Wu, and X. Gao, "Frequency recognition based on canonical correlation analysis for SSVEP-based BCIs," *IEEE Transactions on Biomedical Engineering*, vol. 53, no. 12, pp. 2610–2614, 2006.
- [7] Y. Zhang, G. Zhou, Q. Zhao, A. Onishi, J. Jin, X. Wang, and A. Cichocki, "Multiway canonical correlation analysis for frequency components recognition in SSVEP-based BCIs," in *Neural Information Processing*. Springer, 2011, pp. 287–295.
- [8] Y. Zhang, G. Zhou, J. Jin, M. Wang, X. Wang, and A. Cichocki, "L1-regularized multiway canonical correlation analysis for SSVEP-based BCI," *IEEE Transactions on Neural Systems and Rehabilitation Engineering*, vol. 21, no. 6, pp. 887–896, 2013.
- [9] G. Bin, X. Gao, Y. Wang, Y. Li, B. Hong, and S. Gao, "A high-speed BCI based on code modulation VEP," *Journal of neural engineering*, vol. 8, no. 2, p. 025015, 2011.
- [10] X. Chen, Y. Wang, S. Gao, T.-P. Jung, and X. Gao, "Filter bank canonical correlation analysis for implementing a high-speed ssvep-based brain-computer interface," *Journal of neural engineering*, vol. 12, no. 4, p. 046008, 2015.
- [11] M. Nakanishi, Y. Wang, Y.-T. Wang, and T.-P. Jung, "A comparison study of canonical correlation analysis based methods for detecting steady-state visual evoked potentials," *PLOS ONE*, vol. 10, no. 10, 2015.
- [12] M. H. Chang, H. J. Baek, S. M. Lee, and K. S. Park, "An amplitude-modulated visual stimulation for reducing eye fatigue in ssvep-based brain-computer interfaces," *Clinical Neurophysiology*, vol. 125, no. 7, pp. 1380–1391, 2014.
- [13] R. S. Fisher, G. Harding, G. Erba, G. L. Barkley, and A. Wilkins, "Photic-and pattern-induced seizures: a review for the epilepsy foundation of america working group," *Epilepsia*, vol. 46, no. 9, pp. 1426–1441, 2005.
- [14] W. Yijun, W. Ruiping, G. Xiaorong, and G. Shangkai, "Brain-computer interface based on the high-frequency steady-state visual evoked potential," in *Neural Interface and Control, 2005. Proceedings. 2005 First International Conference on*. IEEE, 2005, pp. 37–39.
- [15] D. D. Muresan and T. W. Parks, "Orthogonal, exactly periodic subspace decomposition," *IEEE Transactions on Signal Processing*, vol. 51, no. 9, pp. 2270–2279, 2003.
- [16] W. A. Sethares and T. W. Staley, "Periodicity transforms," *IEEE Transactions on Signal Processing*, vol. 47, no. 11, pp. 2953–2964, Nov 1999.
- [17] S. V. Tenneti and P. Vaidyanathan, "Nested periodic matrices and dictionaries: new signal representations for period estimation," *IEEE Transactions on Signal Processing*, vol. 63, no. 14, pp. 3736–3750, 2015.
- [18] M. Planat, M. Minarovich, and M. Saniga, "Ramanujan sums analysis of long-period sequences and 1/f noise," *EPL (Europhysics Letters)*, vol. 85, no. 4, p. 40005, 2009.
- [19] L. Mainardi, M. Bertinelli, and R. Sassi, "Analysis of t-wave alternans using the ramanujan transform," in *Computers in Cardiology, 2008*. IEEE, 2008, pp. 605–608.
- [20] S. V. Tenneti and P. Vaidyanathan, "Detecting tandem repeats in DNA using ramanujan filter bank," in *Circuits and Systems (ISCAS), 2016 IEEE International Symposium on*. IEEE, 2016, pp. 21–24.
- [21] P. Saidi, G. Atia, and A. Vosoughi, "Detection of visual evoked potentials using Ramanujan periodicity transform for real time brain computer interfaces," in *IEEE International Conference on Acoustics, Speech and Signal Processing (ICASSP)*, 2017, pp. 959–963.
- [22] —, "On robust detection of brain stimuli with Ramanujan periodicity transforms," in *51st IEEE Asilomar Conference on Signals, Systems and Computers*, 2017.
- [23] L. Zheng and D. N. C. Tse, "Diversity and multiplexing: A fundamental tradeoff in multiple-antenna channels," *IEEE Transactions on information theory*, vol. 49, no. 5, pp. 1073–1096, 2003.
- [24] S. V. Tenneti and P. Vaidyanathan, "A unified theory of union of subspaces representations for period estimation," *IEEE Transactions on Signal Processing*, vol. 64, no. 20, pp. 5217–5231, 2016.
- [25] S. Ramanujan, "On certain trigonometrical sums and their applications in the theory of numbers," *Trans. Cambridge Philosoph. Soc.*, vol. XXII, no. 13, pp. 259–276, 1918.
- [26] P. Vaidyanathan, "Ramanujan sums in the context of signal processing Part I: Fundamentals," *IEEE Transactions on Signal Processing*, vol. 62, no. 16, pp. 4145–4157, 2014.
- [27] —, "Ramanujan sums in the context of signal processing Part II: For representations and applications," *IEEE Transactions on Signal Processing*, vol. 62, no. 16, pp. 4158–4172, 2014.
- [28] H. L. Van Trees, *Detection, estimation, and modulation theory Part I*. John Wiley & Sons, 2004.
- [29] T. W. Anderson and G. P. Styan, "Cochran's theorem, rank additivity, and tripotent matrices," Stanford University, Dept. of Statistics, Tech. Rep. 43, 1980.
- [30] S. J. Press, "Linear combinations of non-central chi-square variates," *The Annals of Mathematical Statistics*, pp. 480–487, 1966.
- [31] W. G. Cochran, "The distribution of quadratic forms in a normal system, with applications to the analysis of covariance," in *Mathematical Proceedings of the Cambridge Philosophical Society*, vol. 30, no. 2. Cambridge University Press, 1934, pp. 178–191.
- [32] H. O. Lancaster and E. Seneta, *Chi-square distribution*. Wiley Online Library, 1969, ch. VII.
- [33] P. Borjesson and C.-E. Sundberg, "Simple approximations of the error function q(x) for communications applications," *IEEE Transactions on Communications*, vol. 27, no. 3, pp. 639–643, 1979.
- [34] K. B. Petersen, M. S. Pedersen *et al.*, "The matrix cookbook," *Technical University of Denmark*, vol. 7, no. 15, p. 510, 2008.